Signatures of Altermagnetism in $BiFeO_3$

Sajid Husain,[1,2,*,†] Maya Ramesh,[3,*] Qian Song,[1,4] Sergei Prokhorenko,[5] Shashank Kumar Ojha,[4,6] Surya Narayan Panda,[4,6] Xinyan Li,[4,6] Yousra Nahas,[5] Yogesh Kumar,[1] Pushpendra Gupta,[1] Tenzin Chang,[2] Alan Ji-in Jung,[2] Rogério de Sousa,[7,8] James G. Analytis,[2] Lane W. Martin,[4,6,9,10] Zhi Yao,[11] Yimo Han,[4,6] Sang-Wook Cheong,[12] Laurent Bellaiche,[5,13] Manuel Bibes,[14] Darrell G. Schlom,[3,15,16] and Ramamoorthy Ramesh[1,2,4,6,9,17,‡]

[1]*Department of Materials Science and Engineering, University of California, Berkeley, California, USA*
[2]*Department of Physics, University of California, Berkeley, California, USA*
[3]*Department of Materials Science and Engineering, Cornell University, Ithaca, New York, USA*
[4]*Department of Materials Science and NanoEngineering, Rice University, Houston, Texas, USA*
[5]*Smart Ferroic Materials Center, Physics Department and Institute for Nanoscience and Engineering, University of Arkansas, Fayetteville, Arkansas 72701, USA*
[6]*Rice Advanced Materials Institute, Rice University, Houston, Texas, 77005, USA*
[7]*Department of Physics and Astronomy, University of Victoria, Victoria, British Columbia, Canada*
[8]*Centre for Advanced Materials and Related Technology, University of Victoria, Victoria, British Columbia, Canada*
[9]*Department of Physics and Astronomy, Rice University, Houston, Texas, USA*
[10]*Department of Chemistry, Rice University, Houston, Texas, USA*
[11]*Applied Mathematics and Computational Research Division, Lawrence Berkeley National Laboratory, USA, Berkeley, California 94560, USA*
[12]*Keck Center for Quantum Magnetism and Department of Physics and Astronomy, Rutgers University, Piscataway, New Jersey 08854, USA*
[13]*Department of Materials Science and Engineering, Tel Aviv University, Ramat Aviv, Tel Aviv 6997801, Israel*
[14]*Laboratoire Albert Fert, CNRS, Thales, Université Paris-Saclay, 91767 Palaiseau, France*
[15]*Kavli Institute at Cornell for Nanoscale Science, Cornell University, Ithaca, New York, 14853, USA*
[16]*Leibniz-Institut fur Kristallzüchtung, Max-Born-Straße 2, 12489, Berlin, Germany*
[17]*Materials Science Division, Lawrence Berkeley National Laboratory, Berkeley, California, USA*

(Received 3 September 2025; revised 15 December 2025; accepted 9 June 2026; published 13 July 2026)

Magnons provide a route to ultrafast transport and nondestructive readout of spin-based information transfer. Here, we report magnon transport and its emergent anisotropic nature in $BiFeO_3$ layers confined between ultrathin layers of the antiferromagnet $LaFeO_3$. Because of the confined state, $BiFeO_3$ serves as an efficient magnon transmission channel as well as a magnetoelectric knob by which to control the stack by means of an electric field. We discuss the mechanism of the anisotropic spin transport based on the interaction between the antiferromagnetic order and the electric field. This allows us to manipulate and amplify the spin transport in such a confined geometry. Furthermore, lower crystal symmetry and suppression of the spin cycloid in ultrathin $BiFeO_3$ stabilizes an antiferromagnetic state exhibiting a nontrivial sign inversion of the spin current, which is a characteristic of an altermagnet. This Letter provides an understanding of the anisotropic spin transport in complex antiferromagnetic heterostructures where ferroelectricity and altermagnetism coexist, paving the way for a new route to realize electric-field control of a novel state of magnetism.

DOI: 10.1103/1wyj-nrgk

Magnons (collective spin excitations) in insulating antiferromagnets (AFMs) offer the potential for ultrafast spin transmission without Joule heating, enabling long-range, nonvolatile collective spin transfer [1–3]. In certain AFMs or two-dimensional ferrimagnets, magnons can transport spin information nonlocally over submillimeter distances [1,4], which is several orders of magnitude larger than typical spin diffusion lengths in metals. This enhanced transport arises from collective excitations and the influence of domain structure [5]. Efficient antiferromagnetic magnon transport in insulating AFMs is based on the transfer of angular momentum, mediated by the Néel vector, the canted magnetic order, or both [1,6]. Traditionally, magnetic fields have been used to control magnon transport in AFMs [1]; however, this method is

*These authors contributed equally to this work.
†Contact author: shusain@berkeley.edu
‡Contact author: rramesh@berkeley.edu

energetically inefficient, and device output voltages are limited by the properties of spin-orbit-coupled metals. More recently, all-oxide heterostructures have emerged as promising platforms for enhancing output voltages [3], as they enable magnon confinement [7] in AFMs and allow for nonvolatile, electric field-based control of magnetism [8].

In this context, a magnetoelectric material, such as $BiFeO_3$ (BFO), which exhibits robust coupling between antiferromagnetic and ferroelectric order at room temperature [9–11], provides a compelling opportunity for electrical control of AFM magnons [12]. It is theoretically proposed that BFO in its noncycloidal (noncollinear [13] or collinear [14]) phase is a promising candidate for hosting a new state of magnetism known as an altermagnetism, which is a recently identified magnetic phase characterized by nonrelativistic spin-split electronic bands. To enable such features, it requires the breaking of the combined $\mathcal{PT}$ and $t\mathcal{T}$ symmetries (where $\mathcal{P}$ is spatial inversion and $\mathcal{T}$ is time reversal), $\mathbf{t}$ is the translational symmetry of the crystal. Ferroelectric materials are natural candidates for realizing such states because their noncentrosymmetric crystal structures inherently break inversion symmetry $\mathcal{P}$, and thus can break $\mathcal{PT}$ when magnetic order is present. In BFO, the octahedral rotations in the rhombohedral $R3c$ phase further lower the symmetry [15] by breaking translational equivalence between Fe sites, effectively breaking the $\mathbf{t}$ symmetry between magnetic moments. This makes BFO a promising platform for altermagnetic behavior [16], but experimental evidence is still lacking. The spin cycloid in BFO needs to be suppressed [16,17] via epitaxial strain [11,18,19], electric field [20,21], rare-earth substitution [10], high magnetic fields [22], or reducing thickness [19]. The intrinsic anisotropy of the electronic band structure of an altermagnet offers a compelling route to probe their magnetic state [23–25], combined with angle-resolved charge/spin transport measurements [6,26].

In this Letter, we report observations of spin transport anisotropy in antiferromagnetic $LaFeO_3/BiFeO_3/LaFeO_3$ (LFO/BFO/LFO) trilayer heterostructures and the signature of an altermagnetism, which can be controlled electrically. We utilize a non-local spin transport (in-plane) device geometry to excite the magnons in the BFO layer via the spin-Hall effect (SHE), and the ISHE is used to detect the response as a function of varying in-plane angles of the nonlocal devices with respect to the substrate crystallographic directions.

Thin film heterostructures of 5 nm LFO/5 nm BFO/5 nm LFO were deposited on $SrTiO_3$ (STO) (001) substrate using molecular-beam epitaxy (End Matter and Supplemental Material, methods [27]). For BFO layers of such thickness, prior work has revealed that the cycloidal magnetic texture is suppressed (Supplemental Material Fig. S1 [27]). In the as-grown state, BFO is found to be an antipolar antiferromagnet. An applied electric field converts this antipolar state into a polar state, accompanied by a ∼100-fold increase in the spin transmission, as probed through inverse-spin-Hall measurements [8]. Such an epitaxial heterostructure forms the model system for us to probe the possibility of an altermagnetic state.

Figure 1(a) depicts the measurement scheme where platinum (Pt) serves as the SHE (source) and ISHE (drain) electrodes. The substrate's in-plane crystallographic axes [Fig. 1(a)] were used as a reference frame to fabricate test structures with systematically varying azimuthal angles, φ, as depicted by the schematic compass in Fig. 1(a) (Fig. S2 [27]). Electric (E) field pulses are applied between the two electrodes to switch the polar (magnetic) state of BFO; Fig. S3(b) [27] shows the comparison of nonlocal ISHE voltage measured as a function of E field in three representative samples: BFO/Pt, LFO/Pt, and the [LFO/BFO/LFO]/Pt. The LFO/Pt does not show an E-field dependence in spin transport [cf. Fig. S3(c) [27]] due to its nonpolar nature, whereas BFO/Pt shows a small spin Seebeck effect, reported previously [2,10]. Figure 1(b) presents an exemplar E field pulsed P employing the PUND (see Fig. S4 [27]) scheme for 0°, 45°, 90°, and 135°, illustrating that there is very little difference in the ferroelectric switching behavior as a function of the azimuthal angle, φ.

An electric field is applied in the $\varphi + 90°$ direction to record the data as a function of azimuthal angles. After this field poling step, the spin transport measurements were carried out on the same set of test structures as in Fig. 1(a) for a range of φ. For a fixed magnitude of supply current (I_{ac}) at the right electrode, the nonlocal inverse-spin-Hall voltage (V_{ISHE}) is recorded (at the left electrode) as a function of the E field [Fig. 1(c)]. The first positive E-field pulse is applied along the [100] direction. The peak-to-peak value (ΔV_{ISHE}) changes as a function of φ, revealing the anisotropic behavior of magnon transport in the heterostructures. Note that the hysteresis polarity reversal occurred in the devices patterned around 135°, characterized by a lower peak-to-peak ISHE voltage magnitude. This sign inversion is the key observation of our Letter, which is likely the experimental evidence of an altermagnetic signature emerging in a BFO-based system, which is consistent with other systems [23–25].

Before we address the altermagnetic origin of the anisotropy and the sign inversion [Fig. 1(c)], we first eliminate other sources of anisotropy such as polarization (P) switching anisotropy, magnetocrystalline anisotropy arising from substrate strain, and the relative orientation of Néel vectors of the two antiferromagnets. First, PUND measurements [Fig. 1(b)] rule out a ferroelectric origin of the observed anisotropy. Second, SQUID magnetometry [Fig. S2(c) [27]] indicates that an in-plane magnetic anisotropy is also not expected. Third, an anisotropic strain should not be a significant factor here due to the cubic symmetry of the STO substrate (See Figs. S6–S9 [27]).

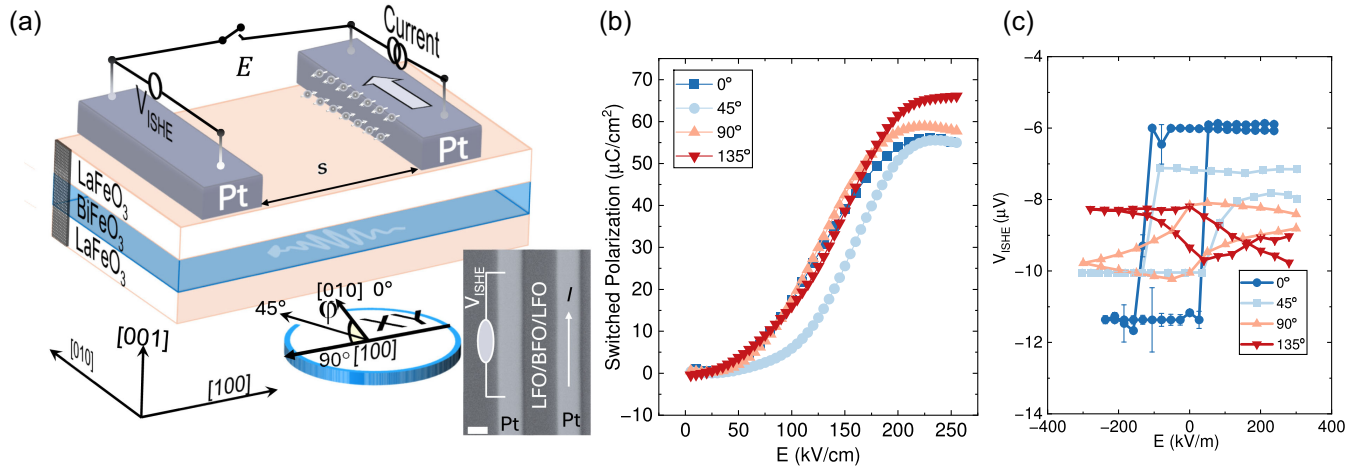

FIG. 1. (a) Device schematic to measure the nonlocal inverse spin Hall effect (ISHE) voltage generated by antiferromagnetic magnons excited through the SHE (gray arrows on the right Pt electrode). Light shaded, wavy arrow, in the BFO middle layer represents the magnon flow direction. φ is the angle between the long axis of the Pt wire and [010], s is the spacing between the metal wires, which is ∼1.5 μm unless otherwise specified. Bottom right is the top view of the device imaged by the scanning electron microscopy, scale bar is 1 μm. (b) Ferroelectric pulsed polarization measured for various devices under the positive-up-negative-down (PUND) scheme. PUND is a standard protocol to record the switched ferroelectric polarization, P, under short electrical pulses (4 μs) and eliminates parasitic contributions to the charge response from resistive leakage and dielectric responses. (c) V_{ISHE} hysteresis measured from the devices with various in-plane angles with respect to the substrate, shown in (a). The hysteresis measured at various angles has been centered with respect to the data measured at 0° to facilitate comparison.

A fourth source of anisotropy involves the relative orientation of the Néel vector in the LFO and the BFO layer (Fig. S10 [27]); this does not explain the sign inversion of the ISHE voltage (Figs. 1 and 2).

We now discuss the angle dependence of the ISHE voltage, shown in Fig. 2(a) for both the pristine and poled state. The data in the pristine state does not show an angle dependence (see Fig. S5 [27]). The data in red, Fig. 2(a), shows the emergence of the anisotropy in the differential ISHE voltage [ΔV_{ISHE}, a difference between the saturated states, Fig. 1(c)] as a function of in-plane angle in the poled state. The data in Fig. 2(b) represent the ΔV_{ISHE} as a function of supply current in the devices patterned around two representative angles, such as $\varphi = 45°$ and 135°. In this panel, positive/negative direct current (Methods, Supplemental Material [27]) gives V_{ISHE} hysteresis with counter-clockwise/clockwise polarity [represented by the curved arrows in Fig. 2(b)], a sign of SHE origin. There is an additional polarity reversal (pink vs turquoise color), which is an emerging signature of altermagnetism in the heterostructure.

The polar and magnetic order parameters viewed down the [111] direction with the glide mirror planes (C_m) are shown in Figs. 3(a) and 3(b). In the device patterned at $\varphi = \sim 0°$, reversing the electric field direction from $[100]_{\mathrm{pc}}$ to $[\bar{1}00]_{\mathrm{pc}}$, switches the **P** in-plane by 71° [from I to II, Fig. 3(c)], which then switches the Néel vector l and canted moment (m) connected through a rotation [11,32]. The output voltage at the detector wire exhibits hysteresis, with the magnitude of the voltage being high or low, depending on the net antiferromagnetic and canted moments sensed by the SHE metal wire [Fig. S9(a) [27]]. Also the fact that what matters is the projects of l and/or m along the direction perpendicular to the Pt wire to generate output voltage. The switching mechanism in the device at $\varphi = \sim 90°$ (i.e., along [100]), is connected by the mirror plane shown by a horizontal dotted line in Fig. 3(c), which gives the minimum change (ΔV_{ISHE}) in spin transport [Fig. S9(b) [27]]. We now apply a similar analysis to the devices around ∼45° and ∼135°, in order to understand the sign inversion observed in Fig. 2(b). Switching (polar/magnetic) operations $I - III$ and $II - IV$ [Fig. 3(c) and Figs. S9(c) and 9(d) [27]] produces an equivalent output voltage in the devices at ∼45° and ∼135°, since these are connected through a mirror operation. However, due to the opposite projection of the net l and/or m around these angles, the output ΔV_{ISHE} will have the opposite sign. In contrast, the Néel vector relationship between the LFO and BFO, in Fig. S10 and in Note S1 and Note S2 [27] does not explain the sign inversion. Under nonequilibrium magnon accumulation, $\nabla(\mu_1 - \mu_2) \neq 0$ (where μ_1 and μ_2 correspond to the spin accumulation due to the sublattice magnetization m_1, and m_2 of an antiferromagnet), the generated nonlocal ISHE voltage, $V_{\mathrm{ISHE}} \propto \cos^2\varphi$, which explains the anisotropic spin transport behavior [Fig. 2(a)]. However, this by itself cannot explain the sign inversion. Therefore, the origin of polarity inversion of the ISHE voltage output shown in Fig. 2 points to the electronic band structure of BFO, i.e., its altermagnetism.

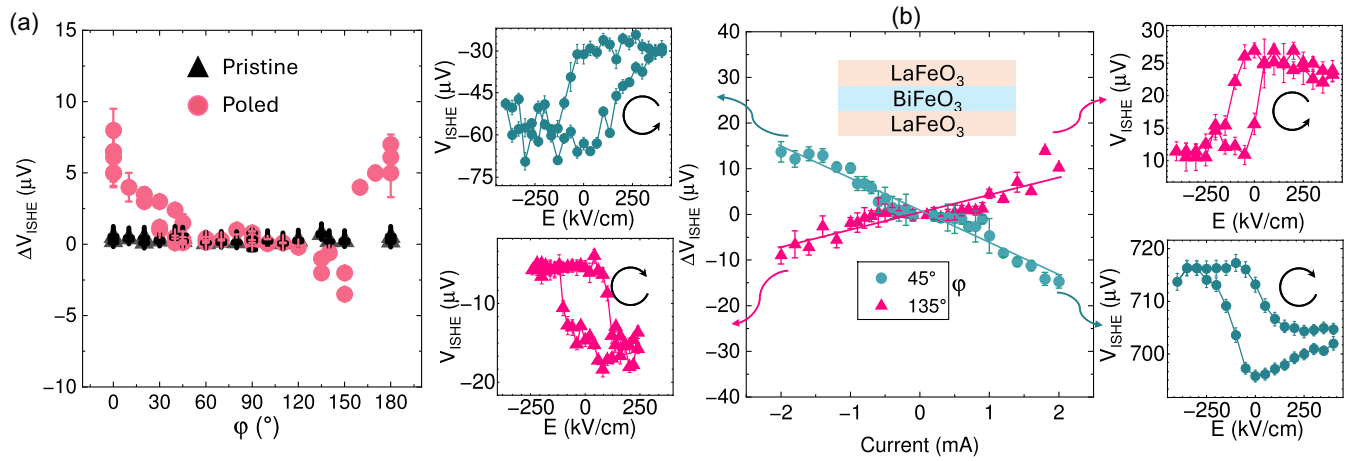

FIG. 2. Differential voltage (ΔV_{ISHE}) as a function of the angle (φ) with respect to the substrate edge [100]. The Pt wires are parallel to [010] and the electric field is applied along $\varphi + 90°$ to measure the polarization and spin transport hysteresis recorded at 0.5 mA. The data in black have been recorded in the pristine state when the electric field was not applied. The pristine state measurements were simply conducted by swapping the source and drain connections (Fig. S5 [27]). The data was recorded from various devices at each angle, represented by several data points plotted at the same angle. From two of these devices, (b) ΔV_{ISHE} as a function of injected current in two devices of $\varphi = 45°$ and $\varphi = 135°$ in the LFO/BFO/LFO trilayer. The sign of the ΔV_{ISHE} gets reversed when the injected current direction is opposite. The hysteresis in the left and right panels is of opposite polarity due to two opposite currents used in the source Pt wire. Similarly, in the orthogonal devices ($\varphi = 45°$ or $\varphi = 135°$), the corresponding hysteresis also shows opposite polarities. The hystereses shown here were measured at a 2 mA supply DC.

The altermagnetism in BFO is intrinsically related to the alternating oxygen octahedra rotations that surround Fe^{3+} ions, thereby breaking the pure translational symmetry between the spin-up and spin-down AFM sublattices. In the $R3c$ phase of bulk BFO, the two G-type AFM sublattices are related by a glide plane that combines translation along

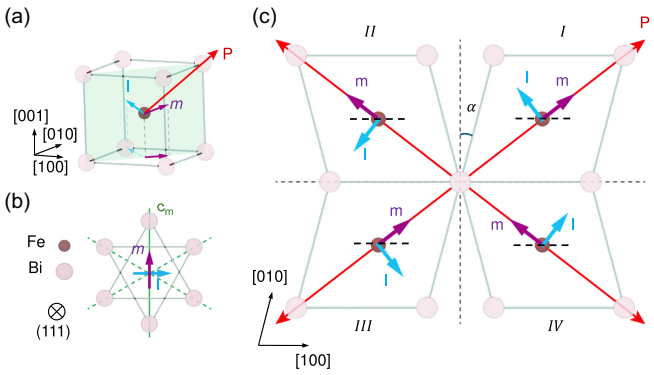

FIG. 3. Description of the anisotropy and sign inversion: (a) Representation of the rhombohedral $R3c$ structure of BFO, illustrating its relationship to the ideal pseudocubic perovskite lattice. The threefold symmetry axis along the pseudocubic [111] direction is marked by a red arrow. (b) A view along the [111] direction. The c_m-glide planes are highlighted with dotted black lines. (c) Top view of the four possible situations of the devices at angles of 0°, 45°, 90°, and 135° being under consideration under poled conditions. α is the tilt due to the noncentrosymmetric $R3c$, l and m are the antiferromagnetic and canted moment of BFO. $I - IV$ correspond to the four four-quadrants that provide access to explain four device angles and connected symmetries.

the [111] axis and a $(1\bar{1}0)$ mirror reflection. As a result, a $(1\bar{1}0)$ mirror operation relating [100] to [010] as well as $[1\bar{1}0]$ and $[\bar{1}10]$ directions (in pseudocubic notation) is intrinsically linked to an inversion of the spin-up and spin-down channels. This argument is supported by our density functional theory calculations (End Matter) presented in Fig. 4. Figure 4(a) depicts the Brillouin zone (BZ) of the $R3c$ phase of bulk BFO with the aforementioned [100], [010], [110] and $[\bar{1}10]$ zone axes corresponding to the F', F, X, and Q high symmetry points at the BZ boundary, respectively. The spin-resolved Kohn-Sham bands computed along the two paths at the boundary of the (001) cross-section of the Brillouin zone [Fig. 4(a)] are shown in Figs. 4(b) and 4(c). The chosen paths are related by a $(1\bar{1}0)$ mirror and, as can be seen from Fig. 4(a), are indeed equivalent up to an inversion of the spin-up and spin-down bands. Such a band splitting is most pronounced within the top valence bands reaching ~0.15 eV in the vicinity of the F and F' points. These calculations support the altermagnetic character of the polar BFO layer. The nonrelativistic band structure showing the three highest energy valence bands in the vicinity of the F' point ([100] direction) for $P\|[111]$ and $P\|[-111]$ (Fig. 5). Spin-up and spin-down channels are shown with red and blue lines. The results show inversion of the band splitting upon reversing the [100] component of polarization by an electric field, a signature of altermagnetism in BFO. We further draw the spin texture (red "up"/blue "down") in Fig. 4(d) to connect and understand the sign of the output signal in the spin transport experiment. The schematics of the spin density differential for the devices at

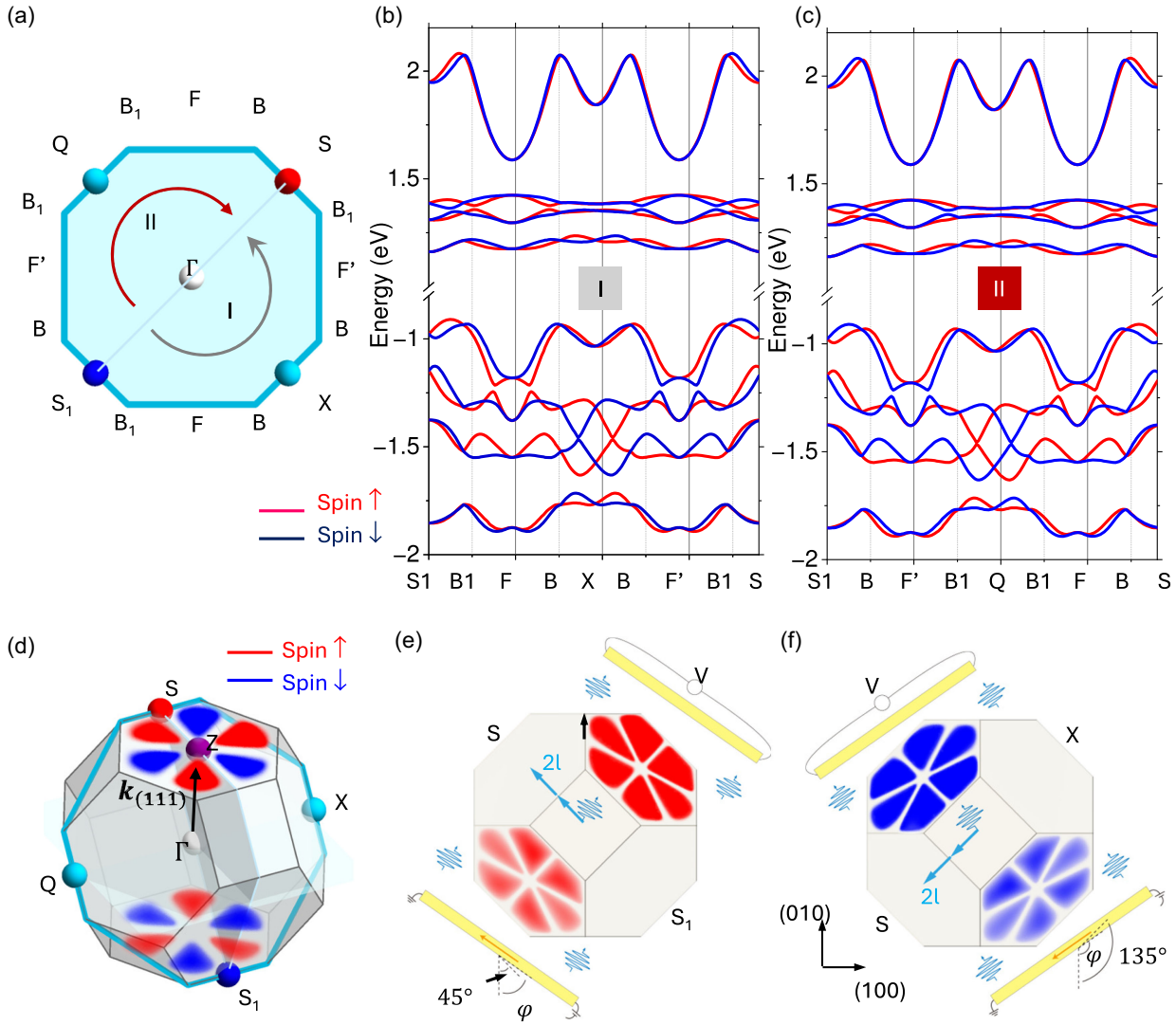

FIG. 4. Anisotropic magnons and emergence of altermagnetism in $BiFeO_3$(BFO) (a) Plane view of the $(001)_{pc}$ Brillouin zone cross section. Two considered k-point paths connecting S and S_1 points lie at the boundary of the Brillouin zone and are related via the $(1\bar{1}0)_{pc}$ mirror plane. Calculated Kohn-Sham band structure of BFO along the two k-point paths shown in panels (b) and (c). Red and blue lines indicate the spin-up and spin-down bands, respectively. (d) First Brillouin zone of the rhombohedral unit cell of $R3c$ bulk BFO with overlapped red and blue spin density bands. Point X corresponds to a $(1\bar{1}0)_{pc}$ mirror image of Q. The corresponding mirror plane containing P, Z, and P_1 points is shown as a gray polygon with light blue edges. Solid blue line passing through S, X, S_1, and Q highlights the boundary of the $(001)_{pc}$ plane cross section of the Brillouin zone. (e),(f) The differential spin texture in the band structure corresponds to the devices patterned at $\varphi = 45°$ and $\varphi = 135°$, respectively. Dark/light color contrast represents the high and low signal, generating the hysteresis between the two polar states.

~45° (red) and ~135° (blue) show the opposite spin contrast [Figs. 4(e) and 4(f)] imprinted on the Pt detectors near these angles, which provides a source of opposite polarity observed in the spin transport when BFO is an altermagnet.

The sign reversal of ΔV_{ISHE} observed across the zero crossing near 45° and 135° indicates that, at these angles, the magnetic order switches to its mirror configuration. For example, around 45°, the P switches from configuration I to III. This P reversal can be viewed as a mirror operation across the (110) plane, as illustrated in Fig. 6 (End Matter). Under this mirror operation, the weak canted moment m—being perpendicular to the mirror plane—remains unchanged, whereas the Néel vector l, which lies within the plane, flips between configurations I and III. The same symmetry relation applies to the devices around 135°, in which magnetic order switches as a mirror operation between configurations II and IV. We also highlight the small rhombohedral distortion, $\alpha \sim 0.6°$, shown in Fig. 3(c). This subtle distortion helps explain why the transformation from configuration I to II [a nearly 90° rotation about (001)] differs from that between II and III (a mirror operation), making the I-II and II-III

switching nonequivalent, shown in Figs. 4(e) and 4(f), a signature of altermagnetism. See also, Figs. S9(c) and S9(d) [27], and End Matter for a detailed description.

In conclusion, we establish a pronounced anisotropy in spin transport within an antiferromagnetic trilayer heterostructure, with a tunable magnon confinement under an applied electric field. We further observe a clear sign reversal in charge-spin interconversion upon in-plane device rotation, providing signatures of an altermagnetic origin in BFO. The intrinsic magnetoelectric coupling suggests the possibility of electric-field control of the altermagnetic phase, linking the emergence and manipulation of altermagnetic order to the ferroelectric state, as supported by first-principles calculations. These results position noncycloidal BFO as a prototypical platform in which altermagnetism and ferroelectricity not only coexist, but are intimately coupled and electrically controllable.

Acknowledgments—This work was supported by the U.S. Department of Energy, Office of Science, Office of Basic Energy Sciences, Materials Sciences and Engineering Division under Contract No. DE-AC02-05CH11231 within the Quantum Materials Program (No. KC2202). S. P., L. B., L. W. M., D. G. S., M. R., and R. R. acknowledge support from the Army Research Office under the ETHOS MURI via cooperative Agreement No. W911NF-21-2-0162 and the Army Research Laboratory under Cooperative Agreement No. W911NF-24-2-0100. S. P. and L. B. additionally acknowledge support from the Vannevar Bush Faculty Fellowship (VBFF) from the Department of Defense, Grant No. W911NF-25-1-0223 from the Army Research Office (ARO) and an Impact Grant 3.0 from ARA. Y. H., L. W. M., and R. R. also acknowledge the support of the National Science Foundation under Grant No. DMR-2329111. R. d. S. acknowledges support of the Natural Sciences and Engineering Research Council of Canada through its Discovery (Grant No. RGPIN-2020-04328). S. W. C. was supported by the DOE under Grant No. DOE: DE-FG02-07ER46382. Z. Y. acknowledges support by the U.S. Department of Energy, Office of Science, Advanced Scientific Computing Research, under Contract No. DE-AC02-05CH11231 within the Exploratory Research for Extreme-Scale Science (EXPRESS) program and the Microelectronics Science Research Centers (MSRC) program.

The views and conclusions contained in this document are those of the authors and should not be interpreted as representing the official policies, either expressed or implied, of the Army Research Laboratory or the U.S. Government. The U.S. Government is authorized to reproduce and distribute reprints for Government purposes, notwithstanding any copyright notation herein.

Data availability—The data that support the findings of this article are not publicly available. The data are available from the authors upon reasonable request.

[1] R. Lebrun, A. Ross, S. Bender, A. Qaiumzadeh, L. Baldrati, J. Cramer, A. Brataas, R. Duine, and M. Kläui, Nature (London) **561**, 222 (2018).
[2] E. Parsonnet, L. Caretta, V. Nagarajan, H. Zhang, H. Taghinejad, P. Behera, X. Huang, P. Kavle, A. Fernandez, D. Nikonov, H. Li, I. Young, J. Analytis, and R. Ramesh, Phys. Rev. Lett. **129**, 087601 (2022).
[3] X. Huang *et al.*, Nat. Mater. **23**, 898 (2024).
[4] X. Y. Wei, O. A. Santos, C. H. Lusero, G. E. Bauer, J. Ben Youssef, and B. J. van Wees, Nat. Mater. **21**, 1352 (2022).
[5] Y. Fan, M. J. Gross, T. Fakhrul, J. Finley, J. T. Hou, S. Ngo, L. Liu, and C. A. Ross, Nat. Nanotechnol. **18**, 1000 (2023).
[6] S. Das, A. Ross, X. Ma, S. Becker, C. Schmitt, F. van Duijn, E. F. Galindez-Ruales, F. Fuhrmann, M.-A. Syskaki, U. Ebels *et al.*, Nat. Commun. **13**, 6140 (2022).
[7] S. Beairsto, M. Cazayous, R. S. Fishman, and R. de Sousa, Phys. Rev. B **104**, 134415 (2021).
[8] S. Husain *et al.*, Nat. Mater. (2026), 10.1038/s41563-026-02531-8.
[9] A. Fert, R. Ramesh, V. Garcia, F. Casanova, and M. Bibes, Rev. Mod. Phys. **96**, 015005 (2024).
[10] S. Husain, I. Harris, P. Meisenheimer, S. Mantri, X. Li, M. Ramesh, P. Behera, H. Taghinejad, J. Kim, P. Kavle *et al.*, Nat. Commun. **15**, 5966 (2024).
[11] A. Haykal, J. Fischer, W. Akhtar, J.-Y. Chauleau, D. Sando, A. Finco, F. Godel, Y. Birkhölzer, C. Carrétéro, N. Jaouen *et al.*, Nat. Commun. **11**, 1704 (2020).
[12] C. Liu, Y. Luo, D. Hong, S. S.-L. Zhang, H. Saglam, Y. Li, Y. Lin, B. Fisher, J. E. Pearson, J. S. Jiang *et al.*, Sci. Adv. **7**, eabg1669 (2021).
[13] S.-W. Cheong and F.-T. Huang, npj Quantum Mater. **9**, 13 (2024).
[14] F. Bernardini, M. Fiebig, and A. Cano, J. Appl. Phys. **137**, 103903 (2024).
[15] L. Šmejkal, J. Sinova, and T. Jungwirth, Phys. Rev. X **12**, 031042 (2022).
[16] A. Urru, D. Seleznev, Y. Teng, S. Y. Park, S. E. Reyes-Lillo, and K. M. Rabe, Phys. Rev. B **112**, 104411 (2025).
[17] D. Sando, A. Barthélémy, and M. Bibes, Nat. Mater. **12**, 641 (2013).
[18] F. Bai, J. Wang, M. Wuttig, J. Li, N. Wang, A. P. Pyatakov, A. K. Zvezdin, L. Cross, and D. Viehland, Appl. Phys. Lett. **86**, 032511 (2005).
[19] P. Dufour, A. Abdelsamie, J. Fischer, A. Finco, A. Haykal, M. F. Sarott, S. Varotto, C. Carrétéro, S. Collin, F. Godel, N. Jaouen, M. Viret, M. Trassin, K. Bouzehouane, V. Jacques, J. Y. Chauleau, S. Fusil, and V. Garcia, Nano Lett. **23**, 9073 (2023).
[20] R. de Sousa, M. Allen, and M. Cazayous, Phys. Rev. Lett. **110**, 267202 (2013).
[21] S. K. Ojha, P. Pal, S. Prokhorenko, S. Husain, M. Ramesh, X. Li, D. Kang, P. Meisenheimer, D. G. Schlom, P. Stevenson, L. Caretta, Y. Nahas, Y. Han, L. W. Martin,

L. Bellaiche, C.-B. Eom, and R. Ramesh, Proc. Natl. Acad. Sci. U.S.A. **122**, e2423298122 (2025).
[22] M. F. Pervez, H. Zhang, Y.-L. Huang, L. Caretta, R. Ramesh, and C. Ulrich, Phys. Rev. B **111**, 174426 (2025).
[23] R. Gonzalez Betancourt, J. Zubáč, R. Gonzalez-Hernandez, K. Geishendorf, Z. Šobáň, G. Springholz, K. Olejník, L. Šmejkal, J. Sinova, T. Jungwirth *et al.*, Phys. Rev. Lett. **130**, 036702 (2023).
[24] D. Jo, D. Go, Y. Mokrousov, P. M. Oppeneer, S.-W. Cheong, and H.-W. Lee, Phys. Rev. Lett. **134**, 196703 (2025).
[25] E. Galindez-Ruales, R. Gonzalez-Hernandez, C. Schmitt, S. Das, F. Fuhrmann, A. Ross, E. Golias, A. Akashdeep, L. Lünenbürger, E. Baek *et al.*, Adv. Mater. **37**, e05019 (2025).
[26] O. Fedchenko, J. Minár, A. Akashdeep, S. W. D'Souza, D. Vasilyev, O. Tkach, L. Odenbreit, Q. Nguyen, D. Kutnyakhov, N. Wind *et al.*, Sci. Adv. **10**, eadj4883 (2024).
[27] See Supplemental Material at http://link.aps.org/supplemental/10.1103/1wyj-nrgk for additional information. Methods for thin film deposition, device fabrication, and spin transport measurements. Device resistance and NV magnetometry imaging on various control samples. Note S1: Understanding the ISHE voltage output and sign inversion. Note S2: Phenomenological understanding of spin Hall effect in the LFO/BFO/LFO trilayers. Role of symmetry and emergence of altermagnetism in the devices. Analytical modeling of anisotropic magnon transport. See also Refs. [28–31].
[28] S. M. Rezende, A. Azevedo, and R. L. Rodríguez-Suárez, J. Appl. Phys. **126**, 151101 (2019).
[29] M. Eibschütz, S. Shtrikman, and D. Treves, Phys. Rev. **156**, 562 (1967).
[30] K. Park, H. Sim, J. C. Leiner, Y. Yoshida, J. Jeong, S.-i. Yano, J. Gardner, P. Bourges, M. Klicpera, V. Se-chovský, M. Boehm, and J.-G. Park, J. Phys. Condens. Matter **30**, 235802 (2018).
[31] J. Sinova, S. O. Valenzuela, J. Wunderlich, C. H. Back, and T. Jungwirth, Rev. Mod. Phys. **87**, 1213 (2015).
[32] P. Meisenheimer, G. Moore, S. Zhou, H. Zhang, X. Huang, S. Husain, X. Chen, L. W. Martin, K. A. Persson, S. Griffin, L. Caretta, P. Stevenson, and R. Ramesh, Nat. Commun. **15**, 2903 (2024).

End Matter

Density functional theory—Density functional theory calculations of the $R3c$ phase of bulk $BiFeO_3$ were performed using Abinit. To simplify the calculation, we chose to use only $BiFeO_3$ as a control layer to demonstrate the altermagnetic state controlled by an electric field. We employ the projector augmented-wave method with Perdew-Birke-Ernzerhof generalized gradient approximation approximation for the exchange correlation functional and U correction on Fe d orbitals of 2 eV. The collinear magnetism is treated at the scalar wave functions level. We use a $6 \times 6 \times 6$ k-point mesh for Brillouin zone integrations and a plane-wave cutoff of 25 Ha, while the cutoff for the double grid is set to 50 Ha. Self-consistent ground-state calculations are performed with a convergence threshold of 10^{-10} Ha. The relaxation of atomic positions is performed until reaching the tolerance for differences of forces of 10^{-6} hartree/Bohr under the assumption of the fixed unit cell geometry given by the rhombohedral lattice constant of 10.639 Bohr and rhombohedral angle of 59.35°. The band structure is computed from a non-self-consistent calculation along the two paths passing through high

TABLE I. Special points along the two considered paths at the boundary of the BZ of $R3c$ BFO. The η value is related to the rhombohedral angle α as $\eta = (1 + 4\cos(\alpha))/(2 + 4\cos(\alpha))$ while $\nu = 3/4 - \eta/2$.

	$\times b_1$	$\times b_2$	$\times b_3$		$\times b_1$	$\times b_2$	$\times b_3$
P_1	$-\eta$	$-\nu$	$-\nu$	P_1	$-\eta$	$-\nu$	$-\nu$
B_1	$-\eta$	-0.5	$\eta - 1$	B	$-\eta$	$\eta - 1$	-0.5
F	-0.5	-0.5	0	F'	-0.5	0	-0.5
B	$\eta - 1$	-0.5	$1 - \eta$	B_1	$\eta - 1$	$1 - \eta$	-0.5
X	0	$-\nu$	ν	Q	0	ν	$-\nu$
B	$1 - \eta$	$\eta - 1$	0.5	B_1	$1 - \eta$	0.5	$\eta - 1$
F'	0.5	0	0.5	F	0.5	0.5	0
B_1	η	$1 - \eta$	0.5	B	η	0.5	$1 - \eta$
P	η	ν	ν	P	η	ν	ν

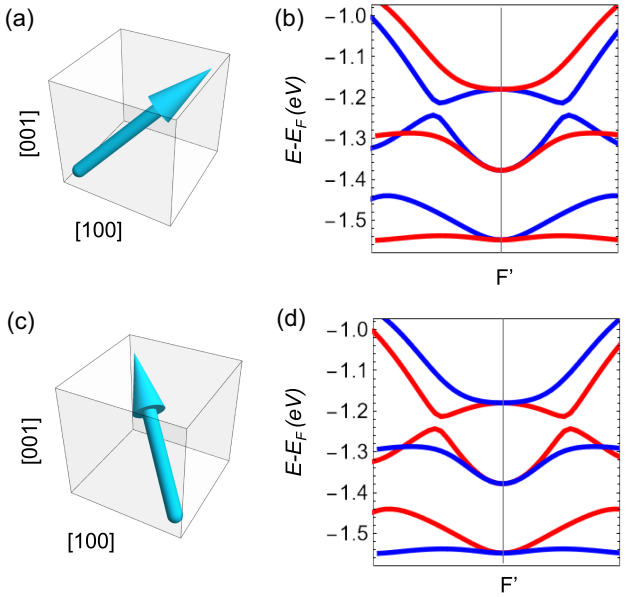

FIG. 5. Computed nonrelativistic band structure showing three highest energy valence bands in the vicinity of F' point ([100] direction) for (a) $P \| [111]$ and (b) $P \| [-111]$. Spin-up and spin-down channels are shown with red and blue lines. The results show inversion of the band splitting upon reversing the [100] component of polarization.

symmetry points listed in the Table I. We also computed the nonrelativistic band structure showing the three highest energy valence bands in the vicinity of F' point ([100] direction) for $P\|[111]$ and $P\|[-111]$ (Fig. 5). Spin-up and spin-down channels are shown with red and blue lines. The results show inversion of the band splitting upon reversing the [100] component of polarization.

Description of the sign inversion under the symmetry of altermagnetic BFO—We first consider whether the Néel vector and weak canted moment contribute to the sign inversion in the ISHE hysteresis shown in Fig. 2. The Néel vector l is oriented perpendicular to the P, as illustrated in Fig. 3(a). This magnetic order belongs to the magnetic space group Cc' [16], featuring a mirror-time-reversal glide plane, shown as green shaded plane in Fig. 3(a). The time reversal symmetry is broken for this magnetic order since the two magnetic sublattices are surrounded by opposite tilt of oxygen octahedral sites, allowing for a weak canted moment induced by spin orbit coupling. The symmetry-allowed direction for the weak canted moment m lies within the mirror-time-reversal glide plane, as shown in Figs. 3(a) and 3(b). In our spin-transport measurements, the ISHE response arises from the spin projected onto the $(100)/(010)$ BFO plane at $\varphi + 90°$ where the φ angle aligned with the Pt electrode. Within this plane, the projected weak canted moment m is parallel to the projected P and perpendicular to the projected Néel vector l. Because the nonequilibrium magnon accumulation $\nabla(\mu_1 - \mu_2) \neq 0$, the two magnetic sublattices are not fully compensated during magnon transport. Therefore, we treat the Néel-vector contribution to magnon transport as an effective net magnetic moment.

The central question in interpreting the ISHE hysteresis is how the magnetic order switches when the P switches. As shown in the angular dependence of the ISHE hysteresis in Fig. 2(a), several angles exhibit zero crossings where ΔV_{ISHE} is negligible. For devices at these angles, the magnetic configuration either remains unchanged or becomes its mirror image when the P switches. These angles cluster near 45°, 90°, and 135°.

The magnetic configurations obtained through the mirror transformations are fully consistent, from a symmetry standpoint, with the observed sign reversal of ΔV_{ISHE} for devices oriented between 45° and 135°. For devices with angles slightly larger than 45°, the switching still

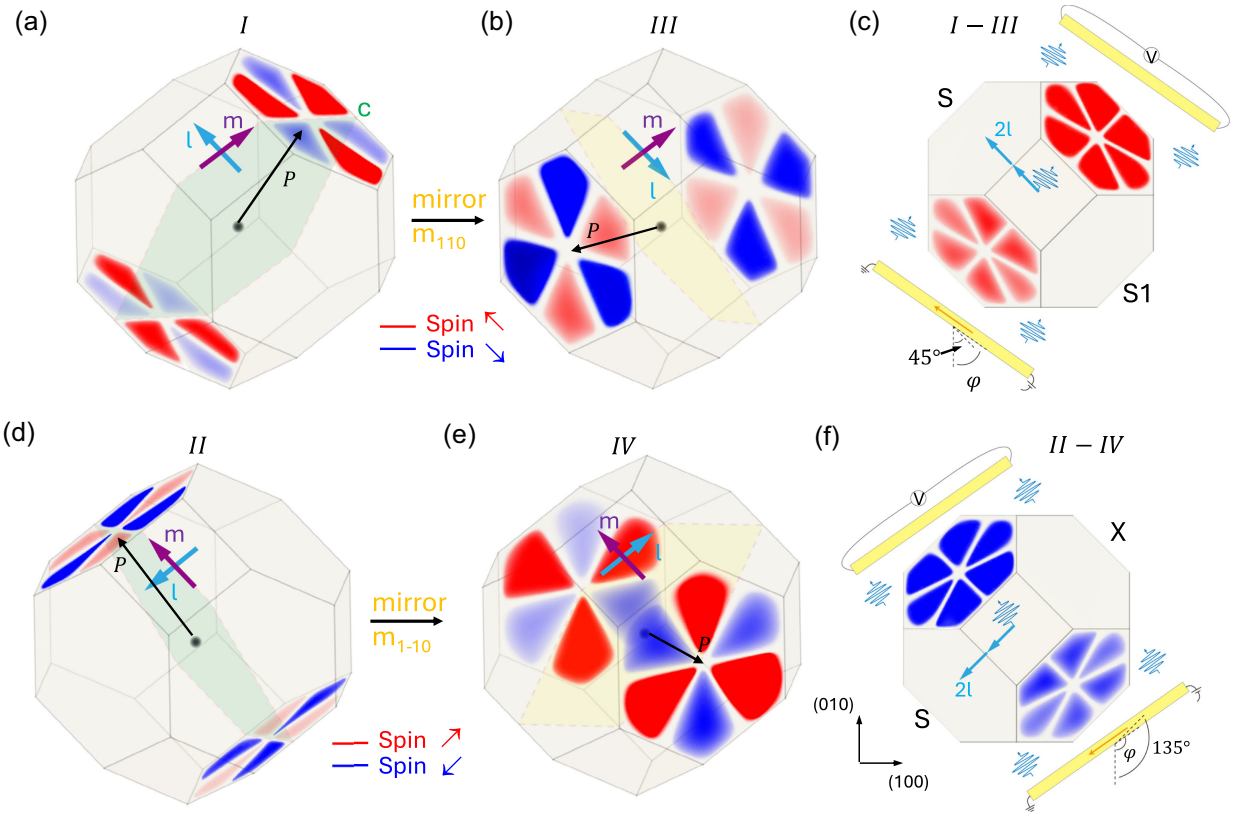

FIG. 6. Possible altermagnetism contribution to the observed sign inversion in the spin transport. Brillouin zone schematic of spin polarization corresponding to 45° *I–III* (a)–(c) and 135° *II–IV* (d)–(f). The green shaded planes in (a), (d) represent the mirror-time-reversal symmetry of Cc' magnetic space group. When the P switches from *I–III* or *II–IV*, the magnetic orders are mirrored, represented by yellow shaded planes in (b), (e). The differential in (c) and (f) show the altermagnetism contribution to ΔV_{ISHE}.

predominantly occurs between configurations *I* and *III*. In this case, the projected canted moment *m* and the Néel vector *l* are parallel to the spin-transport direction in configuration *I* (+*P* state), but antiparallel in configuration *III* (−*P* state). The resulting change in the magnitude of the spin projection produces a difference in the ISHE, leading to a hysteresis with a positive ΔV_{ISHE} during P switching. For devices with angles slightly smaller than 135°, the switching still mainly occurs between configurations *II* and *IV*. Here, the projected canted moment *m* and Néel vector *l* are antiparallel along the spin-transport direction in configuration *II* (+*P* state), but parallel in configuration *IV* (−*P* state). This reversal of *P*, in contrast to the devices oriented slightly larger than 45°, now yields a negative ΔV_{ISHE} during the polarization switching.

The previous discussion focused on the static magnetic-moment contribution to the ISHE, which arises from the spin polarization at the Γ point in the Brillouin zone. The R3c structure BFO with collinear magnetic order is expected to be a g-wave altermagnet. Figure 4(d) presents the g-wave altermagnetic spin texture in the first Brillouin zone for magnetic configuration *I*. The g-wave altermagnetism is protected by the threefold rotational symmetry about the [111] axis and the three mirror planes intersecting the [111] direction, showing three nodal planes in the momentum space spin texture. The spin axes are along the Néel vector direction.

The sign reversal in ΔV_{ISHE} between configurations *I*–*III* and *II*–*IV* was attributed to the antiparallel orientations of the Néel vector *l*. This Néel-vector contribution further suggests that spin polarization away from the Γ point in g-wave altermagnetism may also influence the observed ISHE, since the flowing magnon current shifts the momentum distribution away from Γ. Because the two magnetic sublattices are not fully compensated in magnon transport, we represent the resulting imbalance in spin population using strong and weak color contrasts in our Brillouin-zone illustrations.

For example, Fig. 6(a) shows a stronger red contrast than blue for configuration *I*, reflecting our assumption that spins parallel to the Néel vector contribute more strongly to spin transport and thus have a larger effective filling factor. In configuration *III* [Fig. 6(b)], the Néel vector flips, and consequently the blue contrast becomes stronger than the red. When magnons flow along the (110) direction in configuration *I*, the spins parallel to the Néel vector (red) are preferentially generated, whereas in configuration *III*, the opposite spins (blue) dominate. Effectively, this magnon flow elongates the Néel vector, adding an extra contribution Δl.

This additional contribution, originating from momentum states away from the Γ point, stems from the g-wave altermagnetic spin texture. For devices oriented slightly above 45°, both the Néel vector *l* and the magnon-flow–induced Δl contribute to ΔV_{ISHE}. Subtracting configurations *I* and *III* yields the net difference in the magnon-induced Δl, as illustrated in Fig. 6(c). An analogous situation applies to devices slightly below 135°, which produces a contribution with the opposite sign after subtracting configurations *II* and *IV* [Fig. 6(f)], consistent with the reversed ΔV_{ISHE} dictates the altermagnetic nature of the underlying spin texture. In the magnon transport measurements, magnons with momentum components perpendicular to the transport plane do not contribute. Therefore, the three-dimensional Brillouin zone is projected onto the [100]/[010] plane, as shown in Fig. 6(c). Subtracting the altermagnetic spin textures of configurations *I* and *III* yields a net "red spin texture," reflecting our assumption that spins aligned parallel to the Néel vector contribute more strongly to spin transport. Under this assumption, the resulting spin polarization exhibits the opposite sign for magnetic configurations *II* and *IV*, as indicated by the "blue-colored spin texture" in Fig. 6(f).

SUPPLEMENTAL INFORMATION

Signatures of altermagnetism in $BiFeO_3$

Sajid Husain*

Department of Materials Science and Engineering,

University of California, Berkeley, CA, USA and

Department of Physics, University of California, Berkeley, CA, USA†

Maya Ramesh*

Department of Materials Science and Engineering, Cornell University, Ithaca, USA

Qian Song

Department of Materials Science and NanoEngineering,

Rice University, Houston, TX, USA and

Department of Materials Science and Engineering,

University of California, Berkeley, CA, USA

Sergei Prokhorenko and Yousra Nahas

Smart Ferroic Materials Center, Physics Department

and Institute for Nanoscience and Engineering,

University of Arkansas, Fayetteville, Arkansas 72701, USA

Shashank Kumar Ojha and Surya Narayan Panda

Department of Materials Science and NanoEngineering,

Rice University, Houston, TX, USA and

Rice Advanced Materials Institute, Rice University, Houston, TX, 77005, USA

Xinyan Li and Yimo Han

Rice Advanced Materials Institute, Rice University, Houston, TX, 77005, USA

Yogesh Kumar, Pushpendra Gupta, Tenzin Chang, and Alan Ji-in Jung

Department of Materials Science and Engineering,

University of California, Berkeley, CA, USA

Rogério de Sousa

Department of Physics and Astronomy, University of Victoria,

Victoria, British Columbia, Canada and

Centre for Advanced Materials and Related Technology,

University of Victoria, Victoria, British Columbia, Canada.

James G. Analytis

Department of Physics, University of California, Berkeley, CA, USA[†]

Lane W. Martin

Department of Materials Science and NanoEngineering,

Rice University, Houston, TX, USA

Rice Advanced Materials Institute, Rice University, Houston, TX, 77005, USA

Department of Physics and Astronomy,

Rice University, Houston, TX, USA and

Department of Chemistry, Rice University, Houston, TX, USA

Zhi Yao

Applied Mathematics and Computational Research Division,

Lawrence Berkeley National Laboratory, USA, Berkeley, CA 94560, USA

Sang-Wook Cheong

Keck Center for Quantum Magnetism and Department of Physics and Astronomy,

Rutgers University, Piscataway, New Jersey 08854, USA

Laurent Bellaiche

Smart Ferroic Materials Center, Physics Department

and Institute for Nanoscience and Engineering,

University of Arkansas, Fayetteville, Arkansas 72701, USA and

Department of Materials Science and Engineering,

Tel Aviv University, Ramat Aviv, Tel Aviv 6997801, Israel

Manuel Bibes

Laboratoire Albert Fert, CNRS, Thales,
Université Paris-Saclay, 91767 Palaiseau, France

Darrell G. Schlom
Department of Materials Science and Engineering, Cornell University, Ithaca, USA
Kavli Institute at Cornell for Nanoscale Science,
Cornell University, Ithaca, NY, 14853, USA and
Leibniz-Institut fur Kristallzüchtung,
Max-Born-Str. 2, 12489, Berlin, Germany

Ramamoorthy Ramesh[‡]
Department of Materials Science and Engineering,
University of California, Berkeley, CA, USA
Department of Materials Science and NanoEngineering,
Rice University, Houston, TX, USA
Rice Advanced Materials Institute, Rice University, Houston, TX, 77005, USA
Department of Physics, University of California, Berkeley, CA, USA[†]
Department of Physics and Astronomy,
Rice University, Houston, TX, USA and
Materials Science Division, Lawrence Berkeley National Laboratory, Berkeley, CA, USA

(Dated: June 10, 2026)

* Authors contributed equally
† shusain@berkeley.edu
‡ rramesh@berkeley.edu

CONTENTS

METHODS

Thin film deposition, Device fabrication, and Spin transport measurements: **Thin film trilayer heterostructures** containing $LaFeO_3$ (LFO) and $BiFeO_3$ (BFO) layers were deposited on a $SrTiO_3$ (001) substrate utilizing in-situ reflection high-energy electron diffraction (RHEED) controlled molecular-beam epitaxy (MBE), in a distilled ozone environment serving as the oxidizing agent (80 percent ozone (distilled) and 20 percent oxygen). These layers were grown using elemental sources of either bismuth (Bi) or lanthanum (La) and iron (Fe) at fluxes of 1.5×10^{14}, 2.5×10^{13}, and 2×10^{13} atoms per cm^2/s for Bi, La, and Fe respectively, corresponding to a relative flux ratio of 8:1 for BFO layers and a relative flux ratio of 5:4 for LFO layers. In this regime, the La:Fe flux ratio determines the stoichiometry of $LaFeO_3$. The first layer of LFO was grown at 740 °C and a deposition pressure of 2×10^{-7} Torr. The BFO and second LFO layers were deposited at a substrate temperature of 675 °C, and a chamber pressure of 5×10^{-6} Torr. The substrate temperature was measured using an optical pyrometer at a wavelength of 980 nm, focused on a platinum layer deposited on the backside of the substrate for better thermal conductivity. The structure of the trilayer

heterostructure is LFO(5 nm)/BFO(5 nm)/LFO(5 nm). $SrTiO_3$ was chosen as the substrate for its excellent lattice match to LFO among commercially available substrates, as well as providing isotropic strain (-1.35%) to BFO. As a controlled sample for a normal ferroelectric (no magnetic layer involved) layer, 100 nm thick $Pb_{0.5}Sr_{0.5}TiO_3$ (PSTO) layer was deposited on $DyScO_3$ (110) via pulsed laser deposition using a KrF excimer laser (248 nm). The PSTO growth was carried out at a heater temperature of 650°C in a dynamic oxygen pressure of 100 mTorr with a laser fluence of 1.8 J/cm^2. Following the growth, the sample was cooled to room temperature at 20°C/min, in a static atmospheric oxygen pressure. To understand the anisotropy origin from the substrate strain, a single layer of BFO (80nm) was deposited on different substrates such as $DyScO_3$ (DSO), $TbScO_3$ (TSO), and $SrTiO_3$ (STO), which induces, respectively -0.35 %, -0.1 %, and -1.35 %, strain on BFO.

Post film depositions, **non-local devices** of various angles (0-180° with respect to the substrate edge) (Supplemental Figure 2) were patterned using photolithography using a Maskless Aligner MLA-150. Following exposure, the resist underwent wet-etching using MEGAPOSIT MF-26A photoresist developer for 18 seconds. Subsequently, the Pt (10nm) thin film was deposited for lift-off in the rectangular stripes measuring 100 μm × 1.2 μm. For smaller spacing (Supplemental Figure 3 (c)), 130 keV Crestec tool was used with a 100 keV electron beam, a 600 micrometer field size, 60000 dots, 200 pA dose current. The exposure base time is 1.2 microseconds, and the proximity effect correction factors are calculated using BEAMER software. Before patterning, we carried out spin-coating using PMMA 950 A2, at 3500 rpm for 30 seconds, followed by baking at 180 °C, for 60 seconds. After patterning, it was developed in 3:1 IPA:DI water for 60 seconds. Again, the Pt layers were deposited for lift-off, resulting in the formation of rectangular stripes of dimensions 38 μm × 400 nm.

Spin transport measurements were conducted employing four-terminal non-local de-

vices, wherein two terminals were dedicated to source current injection for the spin Hall effect or supplying a heat gradient to the magnon medium, and the remaining two served as output terminals for inverse spin Hall effect (ISHE) voltage measurements. One source terminal and one detection terminal were also used to apply an electric field for ferroelectric polarization control. The measurements were conducted in the remanent state means no electric field was applied during the measurement. Also, no magnetic field (other than Earth's magnetic field) was applied during these measurements. The entire experimental setup and procedures were controlled using in-house-developed Python code and a Keithley switch box, maximizing repeatability. We utilize both a lock-in amplifier and a nanovoltmeter at the detecting electrode, depending on the measurement type, such as spin Hall or spin Seebeck-based non-local spin transport measurements. Using lock-in-based methods, we separate higher-order contributions in the voltage by measuring higher harmonics. Since magnon spin injection/detection scales linearly with current, I, its magnitude is obtained from the first harmonic signal. Any thermal effects due to Joule heating (quadratic in current) in controlled samples of single-layer BFO with Pt have been detected in the second harmonic signal locked at 7 Hz. This comprehensive setup allowed us to perform accurate and controlled transport measurements (using all automated codes), facilitating the investigation of electric field-controlled non-local voltage measurements. In order to capture the ISHE voltage responses for negative values of the read current, we carried out the measurement with the DC source (Figure 2(b), main text). All the measurements were recorded in the absence of the electric field (remnant state), thus eliminating any interference during the magnon transport. All measurements discussed in this Letter are conducted at room temperature.

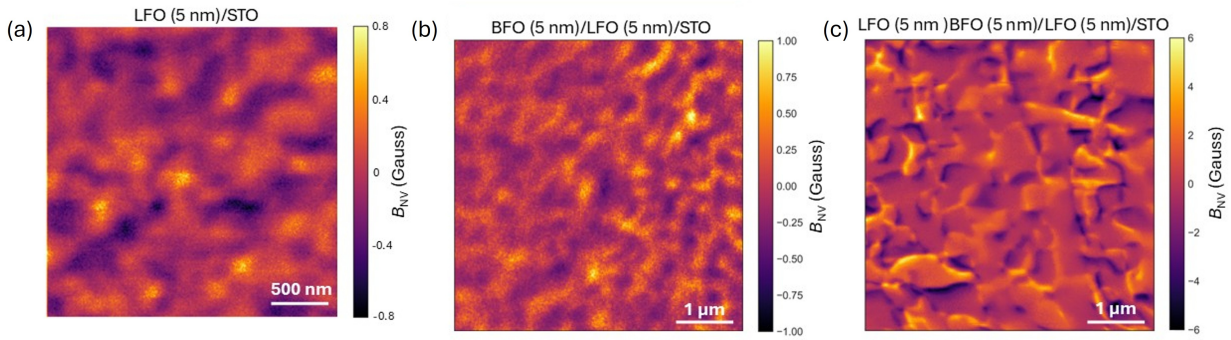

SUPP. FIG. 1. **Magnetic texture recorded in the $BiFeO_3$ (BFO) and $LaFeO_3$ (LFO) thin films using nitrogen vacancy (NV) magnetometry** in (a) LFO(5nm)/STO, (b) BFO(5nm)/LFO(5nm)/STO, and (c) LFO(5nm)/BFO(5nm)/LFO(5nm)/STO.

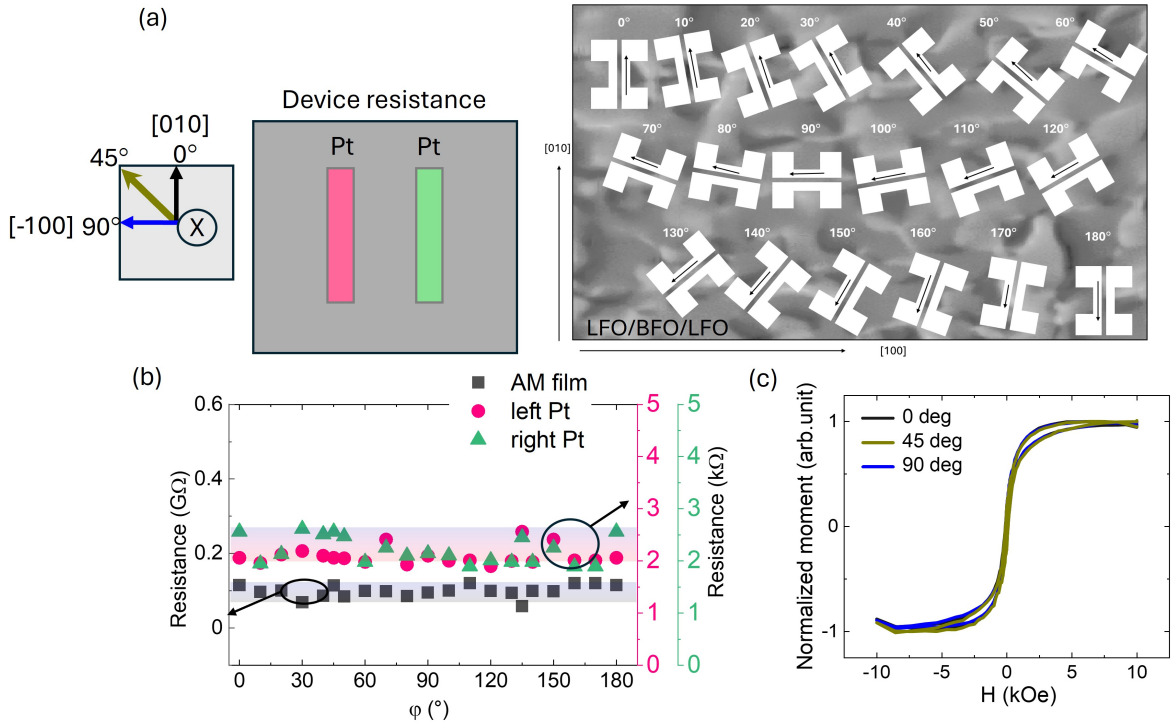

SUPP. FIG. 2. **Device Resistance and anisotropy** as a function of angle. (a) A top view of the device schematic with two Pt wire patterned at fixed spacing with varying angles as shown in the right panel. (b) Resistance of the Pt both left and right wires along with the cross resistance which corresponds to the open circuit resistance being measured by the voltmeter. The data is presented from the devices made from various samples, which added a random fluctuation in the resistance of left and right Pt. (c) Magnetization hysteresis recorded in the sample LFO/BFO/LFO at various angles with respect to the sample edge as described above.

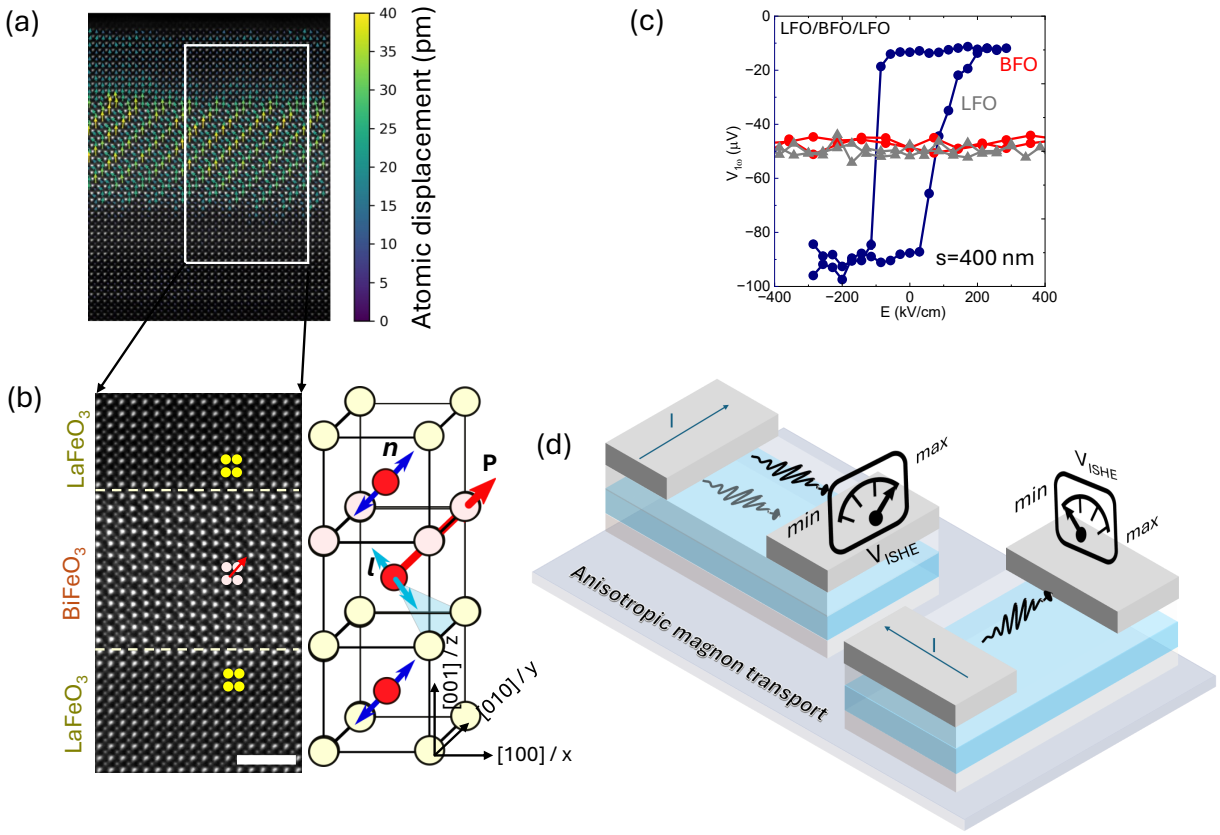

SUPP. FIG. 3. **Anisotropic magnons in $BiFeO_3$(BFO)**. (a,b) High resolution cross-sectional microscopy images of the LFO/BFO/LFO trilayer thin film heterostructure where each layer is 5 nm thick and a schematic depiction of the trilayer, where the BFO has polar (**P**) and antiferromagnetic order $\boldsymbol{l}$ and LFO only exhibits antiferromagnetic order **n**. (c) Typical inverse spin Hall voltage (V_{ISHE}) hysteresis as a function of external field measured in LFO/BFO/LFO trilayer and compared with the single-layer BFO and LFO at an electrode spacing of 400 nm. (d) Depiction of the anisotropic magnon confinement based on the antiferromagnetic environment underneath the spin Hall metal.

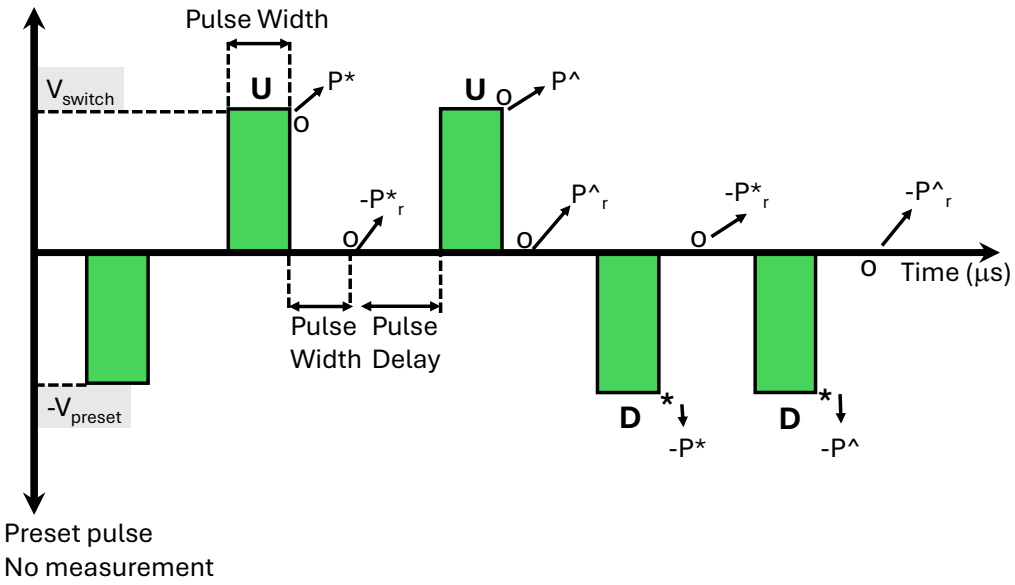

SUPP. FIG. 4. **PUND measurements**. Positive-Up Negative-Down (PUND) measurements were performed at a constant pulse width to determine the ferroelectric polarization of a thin BFO layer sandwiched between LFO layers. This technique employs a sequence of voltage pulses to separate the true polarization switching current from non-ferroelectric contributions such as leakage and dielectric currents, enabling a more accurate evaluation of the sample's ferroelectric properties. The method consists of applying a series of voltage pulses with alternating polarity. A first positive pulse fully polarizes the sample in one direction. This is followed by a negative pulse (P), which switches the polarization. A subsequent positive pulse (U), identical to the previous one, measures only the non-switching contributions (i.e., conduction and dielectric effects), since spontaneous polarization switching no longer occurs. The second pulse aligns the ferroelectric domains in the positive voltage direction and measures the switched polarization. The third pulse repeats the same conditions but captures only the non-remanent polarization and dielectric background, which relaxes during the delay following the second pulse. The fourth and fifth pulses mirror this process for the negative voltage direction, measuring the switched and non-switched polarization, respectively. A delay time of $t = 100\,\text{ms}$ was introduced between pulses to allow for possible back-switching of ferroelectric domains. From these measurements, the quantities $\pm P^*$, $\pm P_r^*$, $\pm P^\wedge$, and $\pm P_r^\wedge$ are obtained. Here, the asterisk $(*)$ denotes the total polarization (remanent plus non-remanent), while the subscript r refers to the remanent component only. Specifically, $+P^*$ $(-P^*)$ is measured at the end of the second (fourth) pulse while the voltage is applied, and $+P_r^*$ $(-P_r^*)$ is measured after a delay of 100 ms once the voltage is removed. Similarly, $+P^\wedge$ $(-P^\wedge)$ is recorded at the end of the third (fifth) pulse during voltage application, and $+P_r^\wedge$ $(-P_r^\wedge)$ is measured after the delay following those pulses. The remanent polarization is calculated as $\Delta P = P^* - P^\wedge$, $\Delta P_r = P_r^* - P_r^\wedge$ and for the negative polarity, $-\Delta P = -P^* - (-P^\wedge)$, $-\Delta P_r = -P_r^* - (-P_r^\wedge)$. All four forms of ΔP yield consistent values of the remanent polarization. By subtracting the current measured during the U pulse from that of the P pulse, the true switched polarization is extracted, as shown in Fig. 1(b) of the main text.

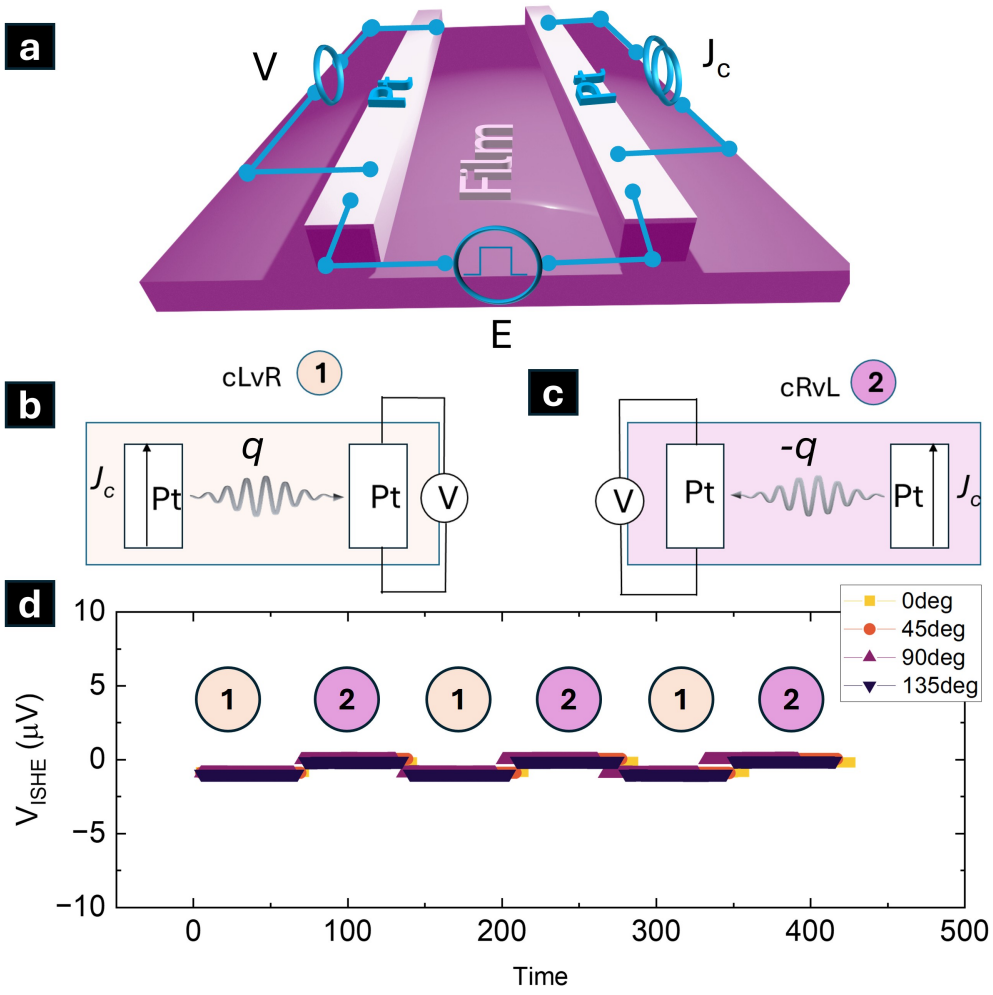

SUPP. FIG. 5. Pristine state non-local magnon voltage measurements in devices with various angles. (a) Non-local device geometry used for the setup with two parallel Pt wires separated by about a micron spacing. (b) and (c) corresponds to the cLvR and cRvL configuration, where the non-local ISHE voltage has been measured for the device without applying an electric field. In these two configurations, we get the asymmetry in the magnon propagating to the left and right as shown in (d).

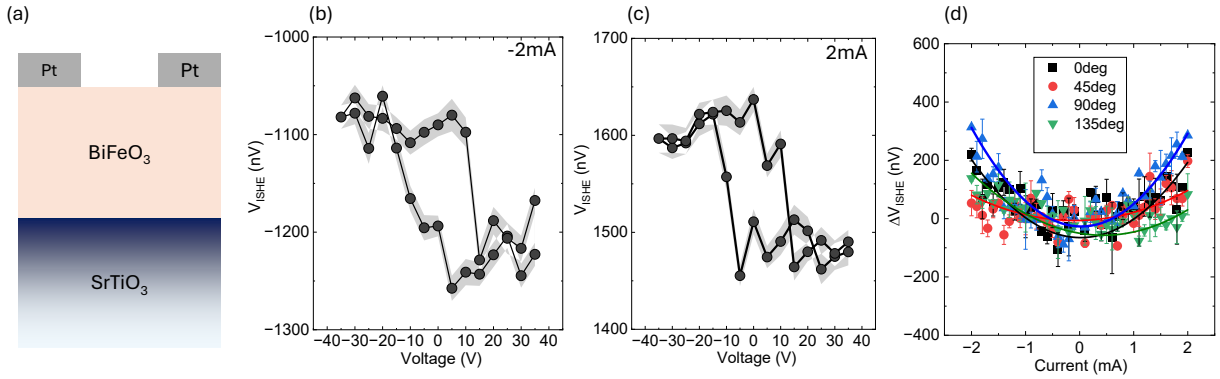

SUPP. FIG. 6. **Angle dependent spin Seebeck in STO/$BiFeO_3$ (80 nm)/Pt(10 nm) device**: (a) Layer schematic with Pt electrodes. (b,c) Non-local voltage V_{ISHE} as a function of electric field recorded at -2mA and 2 mA, respectively. (d) Differential voltage ΔV_{ISHE} recorded by measuring the V_{ISHE} for two opposite poled states. This was done for the device at various angles. Here, we have used a nanovoltmeter detection method where the positive and negative currents were useful to see that the quadratic behavior corresponds to the contributions from the Seebeck effect only. Hysteresis measured at two opposite currents shows that an identical polarity is indicative of the Seebeck effect-induced ISHE voltage. We do not see the sign inversion at any angle, along with negligible anisotropy due to the cubic nature of the STO substrate. This provides strong evidence that the substrate itself does not contribute to the anisotropy and sign inversion observed in the trilayer samples.

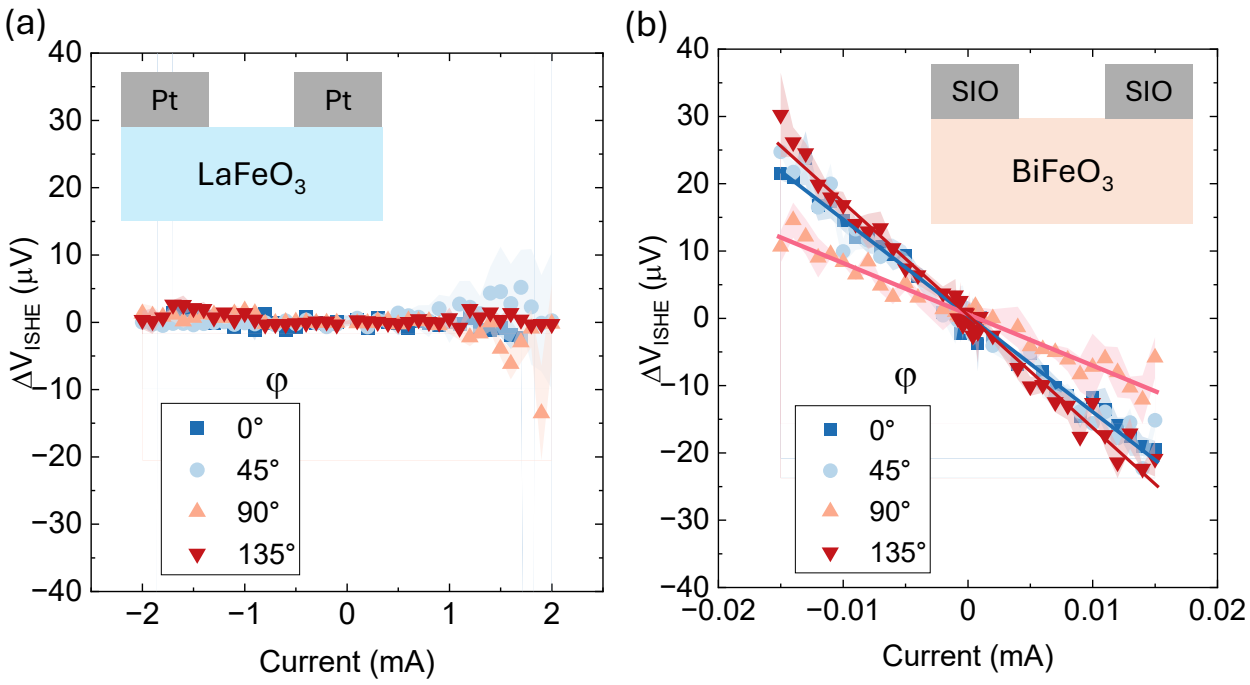

SUPP. FIG. 7. **Spin transport in $SrTiO_3$/$LaFeO_3$(15nm)/Pt(10nm) and $TbScO_3$/$LBiFeO_3$(50nm)/$SrIrO_3$(SIO,10nm):** (a) Differential voltage as a function of the angle (φ) with respect to the substrate crystallographic direction [100] in an LFO single layer, for devices patterned at $\varphi = 0°, 45°, 90°$, and 135°. The E-field-independent behavior indicates the nonpolar nature of the material, as expected. No anisotropy or sign inversion is observed. (b) Differential voltage in $BiFeO_3$ (50 nm)/$SrIrO_3$ (10 nm), where $SrIrO_3$ (SIO) serves as a spin source for magnon excitation in nonlocal spin transport. The measured voltage is significantly higher due to the large spin Hall effect of SIO compared to Pt-based heterostructures (other stacks are discussed in the main text and Supplemental Figures 6 and 8). Nevertheless, a small anisotropy persists, likely due to the finite strain imposed by the orthorhombic $TbScO_3$ substrate.

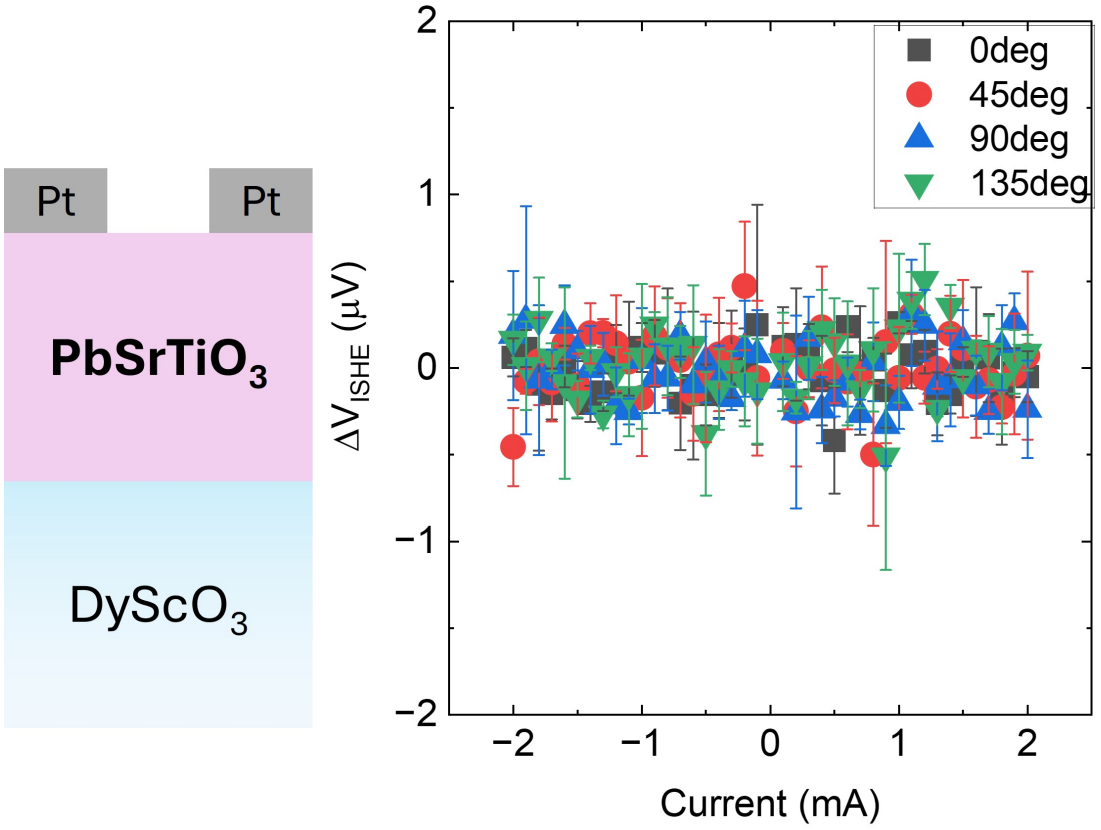

SUPP. FIG. 8. Non-local differential voltage ΔV_{ISHE} as a function of supply current recorded in a ferroelectric sample $DyScO_3/PbSrTiO_3$ (80nm)/Pt (10nm). Note that the absence of a voltage signal in the canonical ferroelectric film here, as measured in the devices prepared at various angles, is indicative of the pure spin source of the voltage signal and the observed anisotropy in the BFO, and LFO/BFO/LFO trilayers samples.

SUPPLEMENTAL NOTE 1

UNDERSTANDING THE ISHE VOLTAGE OUTPUT AND SIGN INVERSION

Fundamentally, the spin Hall effect converts a longitudinal charge current $\mathbf{J}_c$ into a transverse spin current $\mathbf{J}_s \propto \theta_{\mathrm{SH}}(\mathbf{J}_c \times \hat{\sigma})$, where θ_{SH} is the spin Hall angle. The inverse process generates a charge current $\mathbf{J}_c \propto \theta_{\mathrm{SH}}(\mathbf{J}_s \times \hat{\sigma})$. In magnetic systems, the efficiency of spin–charge conversion depends on the relative alignment between the spin polarization $\hat{\sigma}$ and magnetization $\mathbf{m}$ or Neel vector $\mathbf{l}$. Only the component of spin polarization parallel to these magnetic order parameters is efficiently transmitted, while the perpendicular component is absorbed via spin torque. To understand the ISHE conversion and its sign inversion in the devices at various angle along, we draw the schematic shown in Supplemental Figure 9. Here the angles θ_m and θ_l correspond to the angle made by the $\mathbf{m}$ or Neel vector $\mathbf{l}$ with respect to the horizontal axis that contributes to the ISHE conversion. The angle δ is deviation of the device from the 45° and 135°, respectively, where the sign inversion occurs. This angle is a finite deviation from 45° or 135° since the sign inversion is observed around these angle. We define the contributions of the canted moment $\mathbf{m}$ and Neel vector $\mathbf{l}$ on the measurement axes orthogonal to the Pt electrodes according to the right-hand rule. For example, when poled in the P+ state, the voltage output (V_I) is calculated as a projection of $\mathbf{m}$ and $\mathbf{l}$ on the devices at "$\varphi(= 0°) + 90°$" (orthogonal to the length of the wire)

$$V_I \propto (m \cdot cos(\theta_m) - lcos(\theta_m))^2.$$

Similarly for the P- state,

$$V_{II} \propto (m \cdot cos(\theta_m) + lcos(\theta_m))^2.$$

We can formulate these equations for each angle, mentioned in the figure insets.

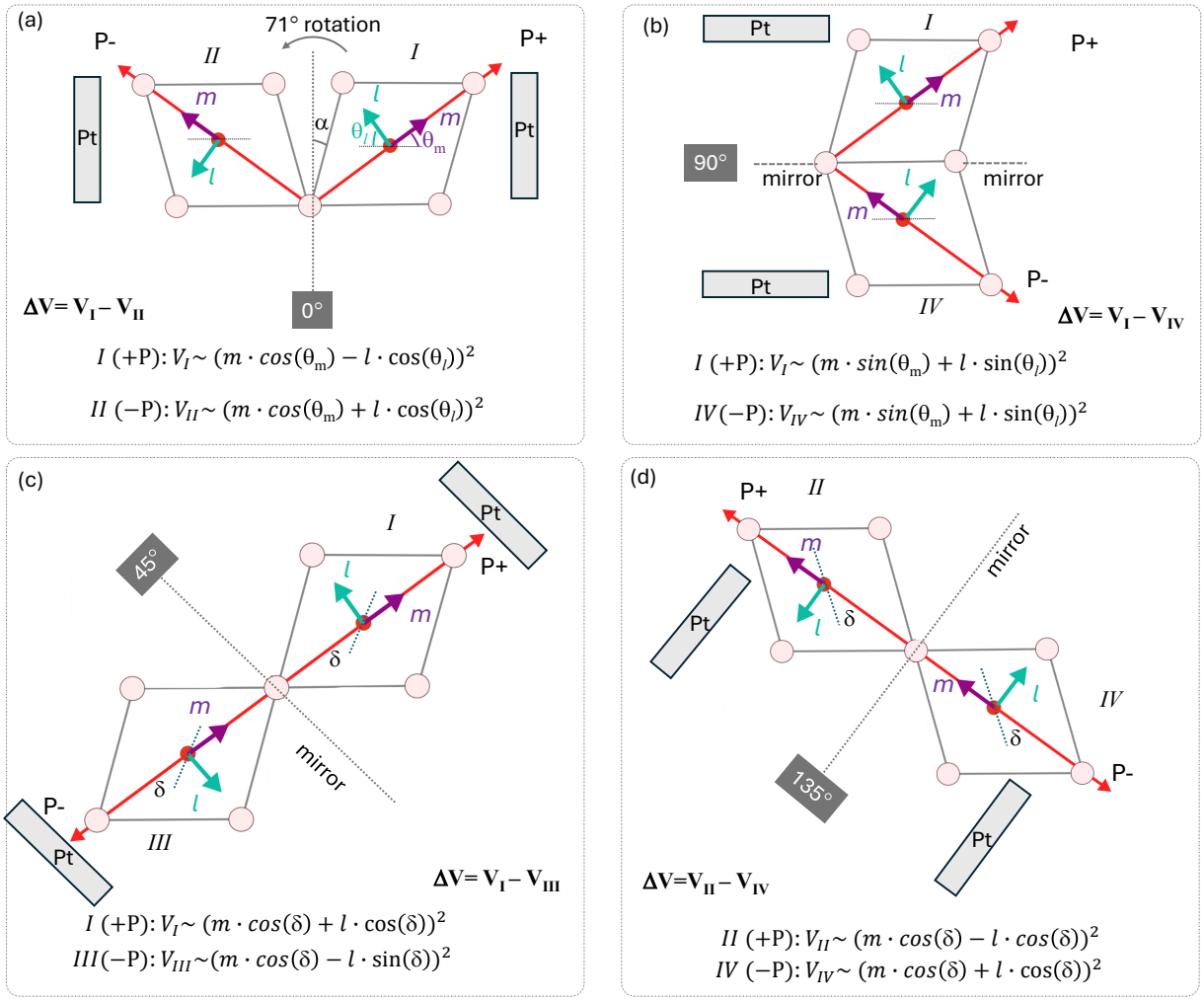

SUPP. FIG. 9. **Anisotropic magnon transport from the symmetry perspective.** (a–d) show the devices in two oppositely poled states, labeled as I, II, III, and IV, corresponding to devices patterned at 0°, 45°, 90°, and 135°, respectively. Under an external electric field, the polarization controls the antiferromagnetic order (l) and the canted moment (m), thereby providing a pathway for the observed anisotropy and sign inversion in spin transport. In (a), the differential signal (ΔV) exhibits the maximum voltage output, while the minimum voltage appears near 90°, as shown in (b). Angles θ_m and θ_l are the angles of canted moment and Neel vector with the axis, which is perpendicular to the Pt electrode. The magnetization/Neel vector projected perpendicular to the Pt electrode contributes to the spin-charge interconversion. Similarly, in (c) and (d), the differential voltages are reversed due to the magnetic configuration, such that $\Delta V(45°) = -\Delta V(135°)$. The angles here are considered to be slightly deviated (δ) from the symmetric plane of 45° and 135°, since the voltage output at exacly these angles will be negligible due to the mirror plane (which can be thought of as a nodal point in the band structure where the splitting is negligible). Therefore the sign inversion emerges slightly away from the symmetry points (Figure 4, main text).

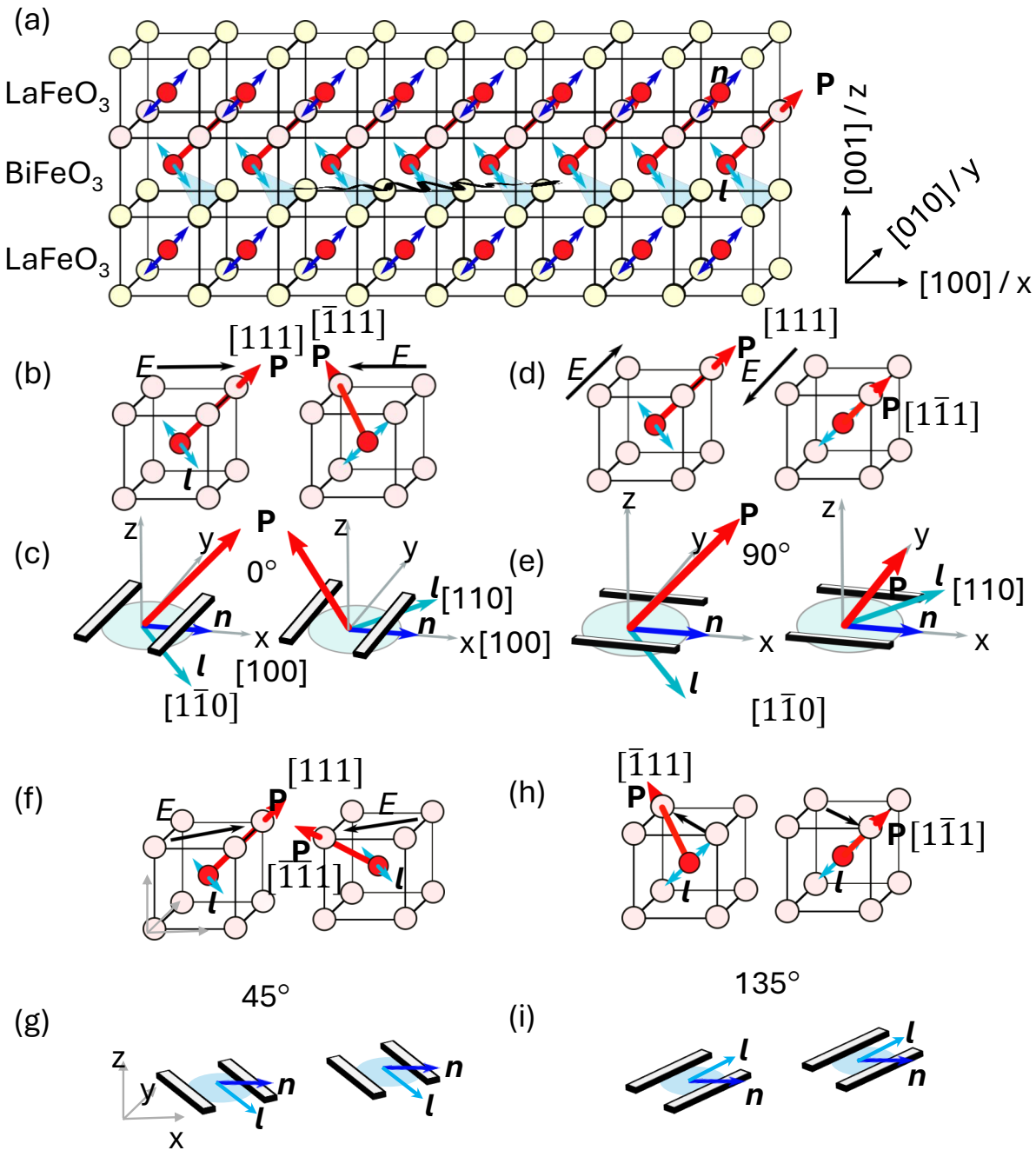

SUPP. FIG. 10. **Anisotropic magnon transport in $LaFeO_3$(LFO)/$BiFeO_3$(BFO)/$LaFeO_3$(LFO)**. (a) Schematic depiction of the trilayer where the BFO has polar (**P**) and antiferromagnetic order $\boldsymbol{l}$ and LFO only exhibits antiferromagnetic order **n**. (b-e) States of the electrical switching of the **P** and $\boldsymbol{l}$ while the **n** remains in the same state due to its non-polar nature. (f,g) and (h,i) Schematic depiction of states of the electrical switching of the **P** and $\boldsymbol{l}$ in the two device orientations. In these two angles (45° and 135°), **P** is switching by 109° in two steps of 71°. For example, P goes from [111] to [$\bar{1}\bar{1}$1] via [$\bar{1}$11] in the device patterned at 45°.

SUPPLEMENTAL NOTE 2

PHENOMENOLOGICAL UNDERSTANDING OF SPIN HALL EFFECT IN THE LFO/BFO/LFO TRILAYERS.

At room temperature, in a diffusive regime, we expect the magnon mean-free path to be smaller than the distance between the injector and detector electrodes for the spin-Hall setup. In that case, the spin current is given by $J_{ij} = -D\partial_i m_j$ where D is the spin diffusion constant and m_j is the j-th component of the magnetization density (note that the spin current is a tensor). A calculation based on the Boltzmann equation, similar to the one applied to non-canted AFMs [1], generalizes the diffusive spin current in a ferromagnet [2] to the case of antiferromagnets with a weak ferromagnetic moment due to canting:

$$\langle \boldsymbol{J}_X \rangle = -\cos(\theta)\frac{g\mu_B}{3V}\sum_{\boldsymbol{q},\alpha=1,2}(-1)^{\alpha}\left(\frac{\partial\omega_\alpha(q)}{\partial \boldsymbol{q}}\right)^2 \tau_{\boldsymbol{q}}\boldsymbol{\nabla} n_B\left(\omega_\alpha(q),\mu_\alpha\right). \tag{1a}$$

$$\langle \boldsymbol{J}_Y \rangle = -\sin(\theta)\frac{g\mu_B}{3V}\sum_{\boldsymbol{q},\alpha=1,2}\left(\frac{\partial\omega_\alpha(q)}{\partial \boldsymbol{q}}\right)^2 \tau_{\boldsymbol{q}}\boldsymbol{\nabla} n_B\left(\omega_\alpha(q),\mu_\alpha\right), \tag{1b}$$

Here $\langle \boldsymbol{J}_X \rangle$ and $\langle \boldsymbol{J}_Y \rangle$ are 3D vectors (not tensors) representing the spin current density related to the modulation of the ferromagnetic moment along X (the direction of the equilibrium Néel vector), and Y (the direction of the weak ferromagnetic moment), see Fig. 11. The angle θ describes the amount of canting which is $<1^\circ$ in orthoferrites [3]. The frequencies $\omega_\alpha(\boldsymbol{q})$ are magnon dispersions for one of the two magnon modes of the AFM ($\alpha = 1, 2$) as a function of $\boldsymbol{q}$, the magnon wavevector, and $n_B(\omega_\alpha(q), \mu)$ is the Bose function:

$$n_B(\omega_\alpha(q),\mu_\alpha) = \frac{1}{e^{\frac{\hbar\omega_\alpha(q)-\mu_\alpha}{k_B T}} - 1}. \tag{2}$$

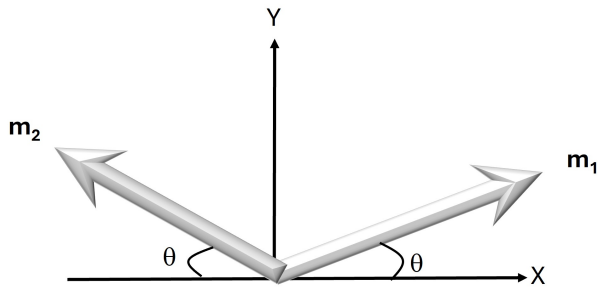

SUPP. FIG. 11. Canted AFM. Directions X and Y correspond to the direction of the equilibrium Néel vector and weak ferromagnetic moment, respectively.

From Eqs. (1a) and (1b) we see that the spin Hall effect happens when there is a spatial gradient in the *differential* chemical potential, $\boldsymbol{\nabla}(\mu_1 - \mu_2) \neq \mathbf{0}$. This is because the sum over $\boldsymbol{q}$ for each magnon mode α describes an integral over a coarse-grained volume of the magnetization $\boldsymbol{m}_i$ in each sublattice of the AFM. The gradients of the Bose functions result in the following expressions:

$$\boldsymbol{\nabla} n_B(\omega_\alpha(q), \mu_\alpha) = \frac{\partial n_B}{\partial \mu_\alpha} \boldsymbol{\nabla}\mu_\alpha = \Sigma_{\alpha=1,2} \frac{1}{k_B T} \frac{e^{\frac{\hbar\omega_\alpha(q)}{k_B T}}}{\left(e^{\frac{\hbar\omega_\alpha(q)}{k_B T}} - 1\right)^2} \boldsymbol{\nabla}\mu_\alpha \,. \tag{3}$$

Combine Eqs. (1a)–(3) to reach the following conclusions:

- Spin Hall effect can be nonzero in collinear AFMs (because spin injection along Néel vector $\boldsymbol{n} = \boldsymbol{m}_1 - \boldsymbol{m}_2$ will increase μ_1 and decrease μ_2, providing the required differential chemical potential). Under the uniform spin accumulations, no spin current can be generated (as discussed in the main text, Figure 2(a) (pristine state)).

- The derivative of the Bose function puts considerable weight on low-frequency magnons. Soft (Goldstone) modes satisfying $\omega_\alpha(q) \to 0$ when $q \to 0$, if present, can potentially give rise to a large spin Hall current. A similar situation happens at high temperatures, when $k_B T \gg K$ where K is the single-ion anisotropy energy per spin. In that

case, the "anisotropy gap" does not impact the value of the spin current.

- Magnon conductivity increases with spin wave velocity. It also increases when the spin wave gap $\hbar\omega_\alpha(q=0)$ decreases, i.e., a reduction in easy-axis anisotropy would lead to larger magnon conductivity.

- With all parameters assumed equal, it can be shown from these equations that a plane of spins ($d=2$, e.g., magnons confined at the interface) gives the same contribution to spin conductivity as a bulk mode ($d=3$). Note we are referring to current density, an intensive quantity, not total current, which is extensive.

Origin of Anisotropy of spin injection/ detection: In bulk $LaFeO_3$ (LFO), the magnetic order is a Néel vector pointing mainly along the (100) direction [4]. If we assume this is also the case for the LFO layers in the LFO/BFO/LFO heterostructure (for both the *Pnma* (non-polar) and *R*3*c* (polar) phases of the BFO layer), then we can predict the angular dependence of spin injection/detection. The key assumption we make in this section is that the Néel vector of the top LFO layer, denoted by $\boldsymbol{n} = \boldsymbol{m}_1 - \boldsymbol{m}_2$, points along the (100) direction at the injector and detector interfaces (Supplemental Figure 10).

An external electric field ($\hat{\boldsymbol{E}}$) between the injector and detector (which is also the DC electric field used to pole from *Pnma* to R_{3c}). The geometry of the injector implies that the injected spins are polarized along $\hat{\boldsymbol{E}}$, see polarized spins in Figure 1(a). Hence, when $\boldsymbol{n} \parallel \hat{\boldsymbol{E}}$ the spin injection will *increase* $\boldsymbol{m}_1$ and *decrease* $\boldsymbol{m}_2$. This in turn will decrease the number of magnons associated to $\boldsymbol{m}_1$ and increase the number of magnons in $\boldsymbol{m}_2$. As a result, $\delta\mu_1 < 0$ and $\delta\mu_2 > 0$. The general argument implies

$$\nabla\left(\mu_1 - \mu_2\right) \propto -\left[\boldsymbol{n}\cdot\hat{\boldsymbol{E}}\right]\hat{\boldsymbol{j}}(\boldsymbol{r}) \propto -\cos\left(\varphi\right)\hat{\boldsymbol{j}}(\boldsymbol{r}), \tag{4}$$

where $\boldsymbol{n}$ is the LFO Néel vector in the region right below the injector electrode, and $\hat{\boldsymbol{j}}(\boldsymbol{r})$ is a unit vector field describing the spin current flow direction (starting from the metal/LFO interface, flowing down through the LFO/BFO, along the BFO channel, and then into BFO/LFO and LFO/metal for spin detection). The first proportionality is general; the second is obtained by assuming $\hat{\boldsymbol{E}} = \cos(\varphi)\hat{\boldsymbol{x}} + \sin(\varphi)\hat{\boldsymbol{y}}$ and $\boldsymbol{n}_I \parallel \hat{\boldsymbol{x}}$, where $\hat{\boldsymbol{x}} = (100)$ and $\hat{\boldsymbol{y}} = (010)$ are cubic crystallographic directions in the LFO/BFO/LFO heterostructure.

We now turn to the physics of the detector electrode. The phenomenological theory of the inverse spin Hall effect predicts that a charge current $\boldsymbol{J}^{(c)}$ emerges when the spin polarization density $\boldsymbol{P}^{(s)} = -\frac{\boldsymbol{M}}{g\mu_B}$ enters the metal detector (See e.g. Section III-B of [5]),

$$\boldsymbol{J}^{(c)} = -\frac{e\alpha_{SH}D}{g\mu_B}\nabla \times \boldsymbol{M}, \tag{5}$$

where α_{SH} is the dimensionless spin-Hall angle and D is the spin diffusion constant. Plugging the diffusive spin current $J_{jk} = -D\partial_j M_k$ we get $J_i^{(c)} = \frac{e\alpha_{SH}}{g\mu_B}\epsilon_{ijk}J_{jk}$ where ϵ_{ijk} is the Levi-Civita tensor with summation over repeated indexes (Einstein's notation).

If we again assume that the LFO Néel vector at the detector region is along x, $\boldsymbol{n}_D \parallel \hat{\boldsymbol{x}}$, we get the following expression for the diffusive spin current right at the interface between LFO and the metal detector: $J_{jk} = -D\partial_j M_x \delta_{k,1} \propto \partial_j(\mu_1 - \mu_2)\delta_{k,1}$. Plug that into $J_i^{(c)}$ and use Ohms's law $J_i^{(c)} = \sigma E_i^{ISHE}$ to get the Inverse spin-Hall effect electric field in the metal detector,

$$\boldsymbol{E}^{ISHE} \propto \frac{e\alpha_{SH}}{g\mu_B\sigma}\nabla \times [(\mu_1 - \mu_2)\hat{\boldsymbol{x}}]\,|_{\boldsymbol{r}_D} = \frac{e\alpha_{SH}}{g\mu_B\sigma}\nabla(\mu_1 - \mu_2)\,|_{\boldsymbol{r}_D} \times \hat{\boldsymbol{x}} \propto \cos(\varphi)\hat{\boldsymbol{y}}. \tag{6}$$

In the last proportionality we assumed Eq. (4) remains valid close to the detector region,

with the spin current direction flowing upwards into the detector, $\hat{\boldsymbol{j}}(\boldsymbol{r}_D) = \hat{\boldsymbol{z}}$. Finally, the ISHE voltage becomes

$$V^{ISHE} = -L_e \left(\hat{\boldsymbol{z}} \times \hat{\boldsymbol{E}} \right) \cdot \boldsymbol{E}^{ISHE} \propto -\cos^2(\varphi). \tag{7}$$

In conclusion, approximate observation of the $\cos^2(\varphi)$ anisotropy in V^{ISHE} implies that the LFO's Néel vector projection is indeed approximately along $\hat{\boldsymbol{x}}$.

[1] S. M. Rezende, A. Azevedo, R. L. Rodríguez-Suárez, *Journal of Applied Physics* **2019**, *126*, 15 151101.

[2] X. Y. Wei, O. A. Santos, C. H. Lusero, G. E. Bauer, J. Ben Youssef, B. J. van Wees, *Nature Materials* **2022**, *21*, 12 1352.

[3] M. Eibschütz, S. Shtrikman, D. Treves, *Physical review* **1967**, *156*, 2 562.

[4] K. Park, H. Sim, J. C. Leiner, Y. Yoshida, J. Jeong, S. I. Yano, J. Gardner, P. Bourges, M. Klicpera, V. Sechovský, M. Boehm, J. G. Park, *Journal of Physics Condensed Matter* **2018**, *30*, 23.

[5] J. Sinova, S. O. Valenzuela, J. Wunderlich, C. H. Back, T. Jungwirth, *Reviews of modern physics* **2015**, *87*, 4 1213.

[6] S. Husain, I. Harris, P. Meisenheimer, S. Mantri, X. Li, M. Ramesh, P. Behera, H. Taghinejad, J. Kim, P. Kavle, et al., *Nature communications* **2024**, *15*, 1 5966.

[7] J. T. Heron, J. L. Bosse, Q. He, Y. Gao, M. Trassin, L. Ye, J. D. Clarkson, C. Wang, J. Liu, S. Salahuddin, D. C. Ralph, D. G. Schlom, J. Íñiguez, B. D. Huey, R. Ramesh, *Nature* **2014**, *516* 370.

[8] S. Husain, M. Ramesh, X. Li, S. Prokhorenko, S. K. Ojha, A. Ross, K. Das, B. Zhao, H. W. Park, P. Meisenheimer, Y. Nahas, L. Caretta, L. W. Martin, S. K. Kim, Z. Yao, H. Wen, S. Salahuddin, L.-Q. Chen, Y. Han, R. de Sousa, L. Bellaiche, M. Bibes, D. G. Schlom, R. Ramesh, *Nature Materials* **2026**, 1–8.

[9] F. Bernardini, M. Fiebig, A. Cano, *Journal of Applied Physics* **2024**, *137*, 10 103903.